DOE/BC/95000169
(DE95000169)

A POPULATION BALANCE MODEL FOR TRANSIENT AND STEADY-STATE FOAM FLOW IN BOISE SANDSTONE

By
A. Kovscek, T. Patzek, and C. Radke

July 1995

University of California
Lawrence Berkeley Laboratory
Berkeley, California

Bartlesville Project Office
U. S. DEPARTMENT OF ENERGY
Bartlesville, Oklahoma

DOE/BC/95000169
Distribution Category UC-122

A Population Balance Model for Transient and Steady-State Foam Flow in Boise Sandstone

By
A. Kovscek,
T. Patzek,
and C. Radke

July 1995

Prepared for
U.S. Department of Energy
Assistant Secretary for Fossil Energy

Thomas Reid, Project Manager
Bartlesville Project Office
P.O. Box 1398
Bartlesville, OK 74005

Prepared by
University of California
Lawrence Berkeley Laboratory
Berkeley, CA 94720

A Population Balance Model For Transient And Steady-State Foam Flow In Boise Sandstone

by

A. R. Kovscek, T. W. Patzek, and C. J. Radke*
Earth Sciences Division of Lawrence Berkeley Laboratory
and Departments of Chemical Engineering and
Material Science and Mineral Engineering
University of California, Berkeley
Berkeley, CA 94720

*Author to whom correspondence should be addressed.

Abstract

An experimental and mechanistic-modeling study is reported for the transient flow of aqueous foam through 1.3-μm^2 (1.3-D) Boise sandstone at backpressures in excess of 5 MPa (700 psi) over a quality range from 0.80 to 0.99. Total superficial velocities range from as little as 0.42 to 2.20 m/day (1.4 ft/day to 7 ft/day). Sequential pressure taps and gamma-ray densitometry measure flow resistance and in-situ liquid saturations, respectively. We garner experimental pressure and saturation profiles in both the transient and steady states.

Adoption of a mean-size foam-bubble conservation equation along with the traditional reservoir simulation equations allows mechanistic foam simulation. Since foam mobility depends heavily upon its texture, the bubble population balance is both useful and necessary as the role of foam texture must be incorporated into any model which seeks accurate prediction of flow properties. Our model employs capillary-pressure-dependent kinetic expressions for lamellae generation and coalescence and also a term for trapping of lamellae. Additionally, the effects of surfactant chemical transport are included. We find quantitative agreement between experimental and theoretical saturation and pressure profiles in both the transient and steady states.

Introduction

During the production lifetime of an oil reservoir, several different recovery processes may be used. For example, water or a gas is injected to maintain reservoir pressure and to drive oil toward production wells. Generally, the most successful processes only recover about 30 to 70% of the oil in place from a reservoir. Ultimate oil recovery is less than 100% because of incomplete volumetric sweep by displacing fluids and because the flow resistance of the displaced oil is proportional to its viscosity. Gases that are typically used as drive agents, such as dense carbon dioxide, nitrogen, and steam, have low viscosities and are highly mobile. They channel selectively through zones of high permeability rather than efficiently displace oil. Further, gas drive fluids are also less dense than crude oil. They migrate to the top of the reservoir and override the oil-rich zones. Thus, traditional gas-displacement processes lack mobility control and result in poor volumetric displacement efficiency due to both channeling and gravity override.

Foam is useful for controlling gas flow in porous media. In reservoir applications, foams are usually formed by nonwetting gases, such as steam, CO_2 or nitrogen, dispersed within a continuous aqueous phase where adsorbed surfactant stabilizes thin liquid films. Nonaqueous foams for gas-mobility control have also been studied for use as gas coning barriers (Hanssen and Haugum, 1991; Hanssen and Dalland, 1990). Foam is relatively cost effective because it is mainly gas and because robust foams may be formed even at low aqueous-phase surfactant concentrations (of order 0.1 to 1 wt%). Since the gaseous portion of foam is dispersed, gas-phase flow resistance is greatly increased and hence gravity override and viscous fingering through high-permeability streaks may be reduced. To date, foams for mobility control in oil recovery processes have not been widely implemented partly because a general understanding and a predictive model of foam flow does not exist.

Most previous laboratory studies of foam flow in porous media were Eddisionian and focused upon the steady state. However, transient flow (*i.e.*, displacement) is the most relevant to enhanced oil recovery. A reliable experimental data set that includes transient pressure and *in-situ* saturation profiles (along the length of a core) at relevant field rates of less than 1 m/day does not exist for foam flow. The most notable attempts at modeling foam flow have focused either on predicting transient flow (Friedmann *et al.*, 1991) or on predicting steady state results (Falls *et al.*, 1988; Ettinger and Radke, 1992), but not both. Additionally, the transient experiments of Friedmann *et al.* (1991) were for rather large gas frontal advance rates between roughly 10 and 1000 m/day.

To elucidate transient foam-flow behavior, we undertook a simultaneous experimental and simulation study of foam displacement. Our goal was to incorporate pore-level foam generation, destruction, and transport mechanisms into a continuum flow displacement model consistent with standard simulation of multiphase flow in porous media (*e.g.*, (Aziz and Settari, 1979; Bear, 1988)) and to verify theoretical results by quantitative comparison to experiment. Here we demonstrate the usefulness and generality of the population-balance approach (Patzek, 1988) for simulating transient and steady-state foam flow in porous media.

The propagation of foam fronts within Boise sandstone at low displacement rates was tracked experimentally under a variety of injection modes and initial conditions. Specifically, three different types of foam displacement were considered: (1) simultaneous injection of gas and surfactant solution at constant mass injection rates into a core completely saturated with surfactant solution, (2) simultaneous injection of gas and surfactant solution into a brine-filled core again at constant mass injection rates, and (3) gas injection into a surfactant-saturated core at fixed injection and exit pressures. Total superficial velocities in the transient mode were generally 1 m/day (3 ft/day) or less. Under steady-state conditions, the liquid flow rate was varied while holding the gas flow rate constant (and *vice versa*) and measuring the resulting pressure-drop behavior.

The interaction of foam with oil is not included here to avoid confusing foam/oil interactions with foam propagation. Once foam propagation in the absence of oil is understood, oil displacement with foam can be included. Foam/oil interactions were studied in parallel with this thesis (Fagan, 1992; Bergeron, 1993; Bergeron *et al.*, 1993). Before describing the flow displacement model, it is helpful to review how foam configures itself within the rock pore space and to understand the pore-level events that alter the size and shape of foam bubbles.

Pore-Level Schematic of Foam Flow

Figure 1 depicts our picture of the pore-level distribution of foam (Chambers and Radke, 1991; Ettinger and Radke, 1992; Kovscek and Radke, 1994; Gillis and Radke, 1990). In this highly schematic picture, cross-hatched circles refer to water-wet sand grains. Wetting surfactant solution is denoted as the dotted phase. Foam bubbles are either unshaded or darkly shaded, depending upon whether they are stationary or flowing. For illustrative purposes only, the largest pore channels lie at the top of the figure while the smallest lie at the bottom.

In compliance with strong capillary forces, wetting liquid occupies the smallest pore space and clings to the surface of sand grains as wetting films. The aqueous, wetting phase maintains continuity throughout the pore structure shown in Fig. 1 so that the aqueous-phase relative permeability function is unchanged in the presence of foam (Bernard *et al.*, 1965; Holm, 1968; Huh and Handy, 1989; De Vries and Wit, 1990; Friedmann and Jensen, April, 1986; Sanchez *et al.*, 1986). Minimal amounts of liquid transport as lamellae. Unshaded flowing foam transports as trains of bubbles through the largest and least resistive flow channels. Because the smallest pore channels are occupied solely by wetting liquid and the largest pore channels carry flowing foam, significant bubble trapping occurs in the intermediate-sized pores.

Foam reduces gas mobility in two ways. First, stationary or trapped foam blocks a large number of channels that otherwise carry gas. Gas tracer studies measure the fraction of gas trapped within a foam at steady state in sandstones to lie between 85 and 99% (Friedmann *et al.*, 1991; Gillis and Radke, 1990). Second, bubble trains within the flowing fraction encounter drag because of the presence of pore walls and constrictions (Falls *et al.*, 1989), and because the gas/liquid interfacial area of a flowing foam bubble is constantly being rearranged by viscous and capillary forces (Hirasaki and Lawson, 1985).

These trains are in a constant state of rearrangement. Foam texture arises through a balance between varied and complicated foam generation and destruction mechanisms. Regardless of whether foam bubbles are generated *in situ* or externally, they are molded and shaped by the porous medium (Chambers and Radke, 1991; Ettinger and Radke, 1992). Bubbles and lamella transport some distance, are destroyed, and then reformed. Further, trains halt when the local pressure gradient is insufficient to keep them mobilized, and other trains then begin to flow. No single bubble or train is conserved over any large distance (*i.e.*, the length of several pore bodies). Bubble trains exist only on a time averaged sense. More thorough reviews of foam generation, coalescence, and transport on the pore level are given by (Chambers and Radke, 1991) and (Kovscek and Radke, 1994).

Experimental Apparatus and Procedures

To quantify the effects of foam on gas and liquid flow, we measure the water content and pressure gradient of a relevant porous medium during displacement at a variety of flow conditions. The centerpiece of the apparatus, displayed schematically in

Fig. 2, is a 60-cm long, 5.1-cm diameter, Boise sandstone core with a permeability of 1.3 μm^2 and a porosity of 0.25 mounted vertically in a stainless steel sleeve. The apparatus is designed to withstand pressures up to 20 MPa (3000 psi). Experiments are conducted at back pressures in excess of 5 MPa (700 psi) and at ambient temperature. *In-situ* measurements of liquid content are provided by gamma-ray densitometry. A translating carriage holding a radioactive ^{137}Cs source and detector allows sampling of the aqueous phase saturation along the entire length of the core. Pressure taps are also located at 10-cm intervals along the core. Pressure is measured by a single Paroscientific 43 KT piezoelectric quartz-crystal pressure transducer (Paroscientific, Redmond, WA) connected to a multiplexing valve (Scannivalve, San Diego, CA). An HP-9000 computer (Hewlett Packard, Co., Mountain View, CA) controls the apparatus and records all data. Further experimental details are available elsewhere (Persoff *et al.*, 1991; Kovscek, 1994; Kovscek and Radke, 1993).

Nitrogen gas and foamer solution are injected at the top of the apparatus. Gas injection is controlled by a 0 to 100 SCCM (standard cubic centimeters per minute) mass flow controller (Emerson Electric, Hatfield, PA) and liquid injection is controlled by a high pressure syringe pump (Instrumentation Specialties Company, Lincoln, NE). Gas superficial velocities span 0.30 to 2.13 m/day (1 to 7 ft/day) at 5 MPa (700 psi) backpressure while liquid velocities as low as 9 mm/day (0.03 ft/day) are possible.

The foamer solution is a saline solution containing 0.83 wt% NaCl with 0.83 wt% active commercial C_{14-16} α-olefin sulfonate surfactant (Bioterg AS-40, Stepan, Anaheim, CA). Water is provided by a glass still. The solution surface tension is 33 mN/m measured by the Wilhelmy plate method, and the solution viscosity is 1 mPa·s. Bottled nitrogen is the gas source.

The core is first flushed with copious amounts (20-100 PV) of 0.83 wt% brine at 7 MPa backpressure. Periodically, the backpressure is released and then reapplied. This treatment removes virtually all gas and surfactant from the core. Because trace amounts of isopropanol or methanol can have a deleterious effect on foam production, no alcohols are used as foam breakers or as cleaning solvents on any portion of the experimental apparatus. For those experiments where the core is presaturated with aqueous surfactant solution, at least 5 PV of foamer solution is injected to satisfy rock adsorption of surfactant. Measurement of the surfactant elution curve for the core during presaturation reveals little detectable surfactant adsorption at the surfactant concentration employed.

After 1 PV of foamer solution is injected, the concentration of surfactant in the inlet and effluent streams is nearly equal (Kovscek, 1994).

The gas/liquid mixture is never foamed before injection and the initial injection rates are not altered until a steady-state pressure drop is achieved. After steady state is reached, the liquid and gas rates are varied independently to reach a series of new steady states. In experiments where gas alone is injected at a fixed inlet pressure, the bone-dry nitrogen stream is first passed through a 0.001 m^3 (1 liter) stainless steel bomb filled with 0.83 wt% brine to saturate the nitrogen with water vapor. In all experiments, the progress of foam propagation is tracked by frequent pressure and saturation sweeps. Discussion of the experimental results is deferred until after description of the foam displacement model.

Foam Displacement Model

The population-balance method for modeling foam flow (Falls *et al.*, 1988; Patzek, 1988) was originally proposed because it incorporates foam into reservoir simulators in a manner that is identical to calculating the transport of mass and energy in porous media. Further, the method is mechanistic in that it can account for the actual pore-level events described in the previous chapters. In its minimal form, the population balance simply adds another component to a standard multicomponent simulator. By analogy to balances on surfactant or other chemical species, a separate conservation equation is written for the number density of foam bubbles. Our goal, in this section, is to map out a population balance that is easy to implement, fits simply into the framework of current reservoir simulators, and employs a minimum of physically meaningful parameters descriptive of the dominant pore-level events. We begin first with the requisite material balance equations for gas, water, surfactant, and foam. Then, equations for foam generation, coalescence, and gas mobility are developed.

Conservation Equations

The mass balance equations for the gaseous and aqueous phases are written in standard reservoir simulator form (*c.f.*, (Aziz and Settari, 1979; Mattax and Dalton, 1990)). For the nonwetting foam or gas phase in a one-dimensional medium we write

$$\frac{\partial[\phi \rho_g S_g]}{\partial t} + \frac{\partial(\rho_g u_g)}{\partial x} = Q_g \qquad (1),$$

where t denotes time and x gives the axial location. ϕ is the porosity of the porous medium, ρ_g is the gas mass density, S_g is the saturation of the gas phase, u_g the superficial or Darcy velocity, and Q_g is a source/sink term for gas used here to apply boundary conditions (Aziz and Settari, 1979). The companion mass balance for the aqueous phase is written by interchanging the subscript g denoting gas for w denoting the liquid phase.

A mass balance on surfactant is also required, which written in standard form becomes

$$\frac{\partial[\phi(C_S S_w + \Gamma)]}{\partial t} + \frac{\partial(u_w C_S)}{\partial x} = Q_S \qquad (2),$$

where C_S is the number or molar concentration of surfactant in the aqueous phase, Γ is the amount of surfactant adsorption on the rock surfaces in units of moles per void volume, and Q_S is the source/sink term for surfactant in units of moles/volume/time.

Since the mobility of the foam phase is a strong function of texture (Hirasaki and Lawson, 1985; Falls *et al.*, 1988; Falls *et al.*, 1989; Chambers and Radke, 1991; Friedmann *et al.*, 1991; Ettinger and Radke, 1992), mechanistic prediction of foam flow in porous media is impossible without a conservation statement accounting for the evolution of foam bubble size (Patzek, 1988). Following Patzek (Patzek, 1988) and others (Falls *et al.*, 1988; Friedmann *et al.*, 1991) we write a transient population balance on the mean bubble size:

$$\frac{\partial[\phi(S_f n_f + S_t n_t)]}{\partial t} + \frac{\partial(u_f n_f)}{\partial x} = \phi S_g(r_g - r_c) + Q_b \qquad (3).$$

In eq. (3), the subscripts f and t refer to flowing and trapped foam, respectively, and n_i is the foam texture or bubble number density. Thus, n_f and n_t are, respectively, the number of foam bubbles per unit volume of flowing and stationary gas. The total gas saturation is given by $S_g = 1 - S_w = S_f + S_t$, and Q_b is a source/sink term for foam bubbles in units of number per unit volume per unit time. The first term of the time derivative is the rate at

which flowing foam texture becomes finer or coarser per unit rock volume while the second is the net rate at which foam bubbles trap. The spatial term tracks the convection of foam bubbles. The usefulness of a foam-bubble population balance, in large part, revolves around the convection of gas and aqueous phases.

On the right of eq. (3), we express generation and coalescence rates, r_g and r_c, on a per volume of gas basis. These two terms are fundamental because they control bubble texture. At steady state, far from any sources or sinks, and where rock properties are constant (*e.g.*, absolute permeability, relative permeability, and capillary pressure functions), bubble size is set by $r_g = r_c$. That is, the rate of bubble generation balances the rate of bubble coalescence (Ettinger and Radke, 1992). To proceed, kinetic expressions are needed for r_g and r_c.

Generation

Snap-off in germination sites underlies the rate expression for bubble generation. Necessary conditions for snap-off, as illustrated in Fig. 3, are the accumulation of liquid at a pore throat (Fig. 3a), a disturbance in the gas liquid interface sufficient to cause breakup and rearrangement of the invading gas thread (Fig. 3b), and displacement of the resulting aqueous lens (Fig. 3c). We neglect foam generation by the bubble leave-behind mechanism (Ransohoff and Radke, 1988). The division mechanism for producing new lamellae yields a rate that is indistinguishable in form from that of coalescence and is included there (Ettinger and Radke, 1992).

Earlier studies (Ransohoff *et al.*, 1987; Falls *et al.*, 1988; Friedmann *et al.*, 1991) argue that the frequency of the snap-off event is inversely proportional to the sum of the time to displace a newly formed lens out of the constriction and the time for wetting liquid to drain back along the pore corners to initiate pinch-off of another lens. By extending the hydrodynamic analysis of Ransohoff *et al.* (Ransohoff *et al.*, 1987) for constricted, cornered pores to include imposed wetting liquid flow along the corners of pores occupied by both gas and wetting liquid, we find (Kovscek, 1994) that the snap-off frequency may be expressed as linearly proportional to liquid velocity and to gas velocity raised to a power less than unity. The liquid-velocity dependence originates from the net imposed liquid flow, while the gas-velocity dependence arises from the time for the lens to exit the pore. Accordingly, we write that

$$r_g = k_1 v_f^a v_w^b \qquad (4),$$

where $v_w = u_w / \phi S_w$ is the local interstitial liquid velocity, and $v_f = u_f / \phi S_f$ is the local interstitial velocity of the flowing foam. These velocities depend upon the local saturation of flowing liquid or gas and the local pressure gradient which can include capillary pressure and gravitational effects; a and b are power exponents, with the index b close to unity. Equation (4) suggests that bubbles are produced only in the portion of the foam that transports. The generation rate constant, k_1, reflects the number of foam germination sites. Intuitively, as liquid saturation falls the number of germination sites falls. We take k_1 as a constant here. Of course, the bubble generation rate does vary implicitly with liquid saturation through the dependencies on liquid and gas velocities. No surfactant properties appear in eq. (4) consistent with the mechanical origin of snap-off.

Others point out that if a lamella (or lens) arrives at a germination site prior to the total elapsed time for snap-off, then snap-off is precluded (Falls *et al.*, 1988; Friedmann *et al.*, 1991). An upper limit is then placed on the evolution of foam texture. We find in our systems that strong coalescence forces come into play before this upper limit is attained.

Some researchers have found a so-called critical velocity for the onset of foam generation (Ransohoff and Radke, 1988; Rossen and Gauglitz, 1990; Friedmann *et al.*, 1991). Friedmann *et al.* (Friedmann *et al.*, 1991) generate foam in sandstone cores at different, initial, surfactant-laden water saturations after steady gas and surfactant-free liquid flow is established. Critical onset velocities increase with decreasing S_w. Velocities up to several hundred meters per day are reported when the initial water saturation is low. Once steady two-phase flow is established, high gas velocities are apparently required for the gas to build a sufficient pressure gradient and enter into wetting, liquid-filled pores.

The existence of a critical velocity for the appearance of strong foam is linked, apparently, to the initial condition of the porous medium. Recent experiments in glass beadpacks, and in Boise and Berea sandstones have not confirmed that a critical gas velocity or pressure drop must be exceeded for successful foam generation (Ettinger, 1989; Persoff *et al.*, 1991; Fagan, 1992; Kovscek and Radke, 1993; Kovscek *et al.*, 1993; Chou, 1991). In all of these cases the porous media were completely saturated with surfactant solution prior to any gas injection. With initial high water saturations foam readily generates. In the experiments and modeling calculations to follow, the initial

water saturation is 100 %. For this reason we do not include a critical onset velocity or pressure gradient in eq. (4).

Coalescence

A pore-level based rate expression for capillary-suction coalescence is readily obtained. Figure 4 illustrates that foam lamellae are destroyed in proportion to their flux (*i.e.*, $v_f n_f$) into termination sites (Jiménez and Radke, 1989). Hence, we write that

$$r_c = k_{-1}(P_c)\, v_f n_f \qquad (5),$$

where $k_{-1}(P_c)$ is a coalescence rate constant that varies strongly with the local capillary pressure, P_c, and n_f is again the number of bubbles per unit volume of the flowing foam. Additionally, the coalescence rate constant also varies with surfactant concentration and formulation. Equation (5) and Fig. 4 teach that higher interstitial gas velocities lead to increased foam coalescence because rapidly stretched lamellae are more vulnerable to breakage. Sufficient time does not exist for surfactant solution to flow into a rapidly stretched lamella and heal it.

Foam coalescence depends upon how effectively a surfactant stabilizes foam lamellae. Weak surfactants and/or low concentrations do not provide adequate stabilization and make $k_{-1}(P_c)$ quite large. The ability of a lamella to withstand large suction capillary pressures before rupturing catastrophically is determined primarily by the molecular structure and concentration of the surfactant. The number of coalescence sites reflected in $k_{-1}(P_c)$ depends strongly upon the capillary pressure applied to lamellae. Khatib *et al.* (1988) have shown that for strongly foaming solutions $k_{-1}(P_c)$ is small for high aqueous phase saturations which imply low capillary pressures, but rises steeply as S_w declines and P_c increases to a value corresponding to the limiting capillary pressure, P_c^*. The limiting capillary pressure refers to the characteristic value of P_c that a porous medium approaches during strong foam flow for a given type and concentration of surfactant solution. P_c^* is interrelated to the rupture disjoining pressure, Π_{rup} of single foam films (Aronson *et al.*, 1994). Surfactant solutions that produce foam films with large rupture disjoining pressures produce strong foams in porous media and high values of the P_c^*.

As the medium capillary pressure approaches the limiting capillary pressure, $k_{-1}(P_c)$ approaches infinity. Cognizant of these observations, we write that

$$k_{-1}(S_w) = k^o_{-1}\left(\frac{P_c}{P_c^* - P_c}\right)^2 \qquad (6),$$

where k^o_{-1} is a scaling constant. Equation (6) allows the coalescence rate to increase monotonically as P_c increases while the porous medium desaturates. As desired, the coalescence rate becomes infinite at P_c^*. It is important to emphasize that the sensitivity of foam to surfactant formulation is embodied in P_c^*. Foamers with high critical rupture disjoining pressures result in high limiting capillary pressures. The capillary pressure curve for the particular medium then sets a low value of S_w^*, the aqueous saturation corresponding to the limiting capillary pressure and, accordingly, a low foam mobility.

Figure 5 displays qualitatively the dependence of both coalescence and generation rates on the wetting liquid saturation and hence capillary pressure. S_w^* may be either smaller or larger than the connate water saturation depending on the surfactant formulation and the nature of the porous medium. Near S_w^*, the rate of foam coalescence rises steeply as P_c approaches the limiting capillary pressure. The intersection of the two rate curves determines the relationship between the steady-state liquid saturation and foam texture from eqs. (4) through (6). It is readily argued that the intersection of coalescence and generation rates in Fig. 3 leads to a stable steady state. If the system is perturbed away from this point, it naturally returns. Consider a small, positive perturbation in the local liquid saturation. The coalescence rate then declines and the foam texture becomes finer. This causes an increased flow resistance, which then returns the liquid saturation back to the stable operating point. The converse negative saturation perturbation is similarly argued to be stable.

Because P_c^* varies with surfactant concentration, another function is necessary for simulations where the porous medium is not presaturated with surfactant. Recent work by Aronson *et al.* (1994) measured pressure drop in 2.3-μm^2 beadbacks for N_2 foams at a gas fractional flow of about 90% and also Π_{rup} for single foam films at a variety of surfactant (sodium dodecyl sulfate) and brine (NaCl) concentrations. This work showed that at elevated brine concentrations (roughly 1 wt%) even small concentrations of surfactant (0.03 wt%) produced substantial beadpack pressure drops and large rupture pressures for single foam films. The following function for P_c^* at high brine concentrations is suggested by their work

$$P_c^* = P_{c,max}^* \tanh\left(\frac{C_s}{C_s^o}\right) \qquad (7),$$

where $P^*_{c,max}$ is a limiting value for P_c^* and C^o_s is a reference surfactant concentration for strong net foam generation. This function allows P_c^* to increase rapidly and smoothly from zero as the surfactant concentration increases and finally to plateau. Hence, P_c^* is small when C_s is small and consequently the rate of coalescence is large and foam cannot form.

The rate of bubble division, the second mechanism for creating foam, is proportional to the flux of lamellae into division sites (Ettinger and Radke, 1992). Thus, the rate of foam generation by division is formally identical to eq. (5). Further, both rate constants share the property of being small when P_c is low, since more division sites become available as P_c climbs. It is thus difficult to distinguish between division and coalescence when writing mechanistic rate expressions. We do not do so here. Additionally, equating capillary-suction coalescence and bubble-division generation rates teaches that, if division is the primary foam generation mechanism, foam texture at steady state is independent of gas rate. This is not the experimental result in permeable sandstones and beadpacks (Khatib *et al.*, 1988; Ettinger, 1989; Ettinger and Radke, 1992). Finally, as gas diffusion coarsening of trapped foam bubbles is restricted in porous media due to the presence of pore walls, we do not include it in our current simulations (Kovscek and Radke, 1994; Rossen, 1994).

Gas Mobility

In addition to bubble kinetic expressions, the mass balance statements in eqs. (1) through (3) demand flow-rate relationships for the foam and wetting liquid phases. From our discussion of Fig. 1, the confined foam is divided into intermediate wetting trapped and nonwetting flowing portions. For the flowing foam, the structure of Darcy's law is retained:

$$u_f = \frac{K\, k_{rf}}{\mu_f}\left(\frac{-\partial p_g}{\partial x}\right) \qquad (8),$$

where K is the absolute permeability, k_{rf} is the relative permeability to the flowing foam, and μ_f is the foam effective viscosity. Equation (8) does not imply Darcy flow because μ_f

is not a constant. Based on the theoretical studies of Bretherton (1961) and Hirasaki and Lawson (1985), we adopt the following expression for the non-Newtonian foam effective viscosity:

$$\mu_f = \mu_g + \frac{\alpha n_f}{v_f^c} \qquad (9),$$

where α is a constant of proportionality dependent primarily on the surfactant system. Others have written similar expressions (Falls *et al.*, 1988; Friedmann *et al.*, 1991; Ettinger and Radke, 1992). According to eq. (9), foam viscosity increases with finer textured foams but decreases with increasing interstitial velocity. In the absence of flowing foam bubbles (i.e., $n_f = 0$) the gas viscosity of a continuous foam is recovered. Friedmann *et al.* (1991) report an empirical value of 0.29 for the exponent c. The Bretherton-based theoretical value is 1/3 (Bretherton, 1961; Hirasaki and Lawson, 1985; Falls *et al.*, 1989; Ginley, 1989; Wong *et al.*, submitted 1993).

Again, since the portion of foam that actually flows partitions into the largest and, hence, least resistive channels while the trapped fraction partitions into the intermediate-sized pores, and wetting liquid flows in the smallest most resistive channels (*cf.*, Fig. 1), a Stone-type model (Stone, 1970) for relative permeability is appropriate. That is, the relative permeability of the most nonwetting phase (*i.e.*, flowing foam) is a function of the saturation of the most nonwetting phase. In accordance with Stone (1970) we write for our foamed-gas and aqueous solution system that

$$k_{rf} = k_{rg}^{o} S_{fd}^{g} \qquad (10a),$$

where

$$S_{fd} = X_f (1 - S_{wd}) \qquad (10b),$$

and

$$S_{wd} = \frac{(S_w - S_{wc})}{(1 - S_{wc})} \qquad (10c).$$

$X_f = S_f/S_g$ is the fraction of the foam phase that is flowing. Flowing foam relative permeability is a function of the saturation of flowing gas and, consequently, is greatly reduced compared to the case of a free gas propagating through the porous medium at the same total gas saturation. Standard Corey exponent models are adopted for the relative permeability functions with g representing the exponent for gas flow (Corey, 1954). The subscript d indicates that the aqueous-phase saturation is normalized over the saturation range where two-phase flow occurs. S_{wc} is the connate aqueous phase saturation, and k^o_{rg} is the gas relative permeability at S_{wc}. k_{rf} (=k_{rg}) is obtained from relative-permeability measurements for continuum gas-liquid flow in the porous medium.

Consonant with Fig. 1, Stone's model for relative permeability also implies that the relative permeability for the aqueous wetting phase is unaffected by the presence of foam. Hence, Darcy's law in eq. (8) is written for the wetting liquid with

$$k_{rw} = k^o_{rw} S^f_{wd} \qquad (11),$$

where k^o_{rw} and f are the Corey scaling constant and exponent for liquid flow, respectively. Recall that this framework confirms the experimental result that during foam flow the aqueous phase distributes into its own separate wetting channels (Bernard and Holm, 1964; Bernard *et al.*, 1965; Holm, 1968; Huh and Handy, 1989; De Vries and Wit, 1990; Friedmann and Jensen, 1986; Sanchez *et al.*, 1986). Again, $k_{rw}(S_w)$ is known from studies on continuum two-phase flow in the medium.

Clearly, the relative permeability of the trapped foam is zero. However, knowledge of the fraction of foam trapped in the porous medium is needed to complete the flow model. In general, the fraction of foam trapped, $X_t = S_t/S_g$, is a function of pressure gradient, capillary pressure, aqueous-phase saturation, and pore geometry. So far, the trapped gas fraction has only been measured for experimental systems at steady state (Friedmann *et al.*, 1991 ; Gillis and Radke, 1990). We write the trapped fraction as a function of the trapped texture, n_t:

$$X_t = X_{t,max}\left(\frac{\beta n_t}{1+\beta n_t}\right) \qquad (12),$$

where $X_{t,max}$ is the maximum fraction of trapped foam, and β is a trapping parameter. Equation (12) demands no trapping when the trapped texture is zero and a smooth rise to

a maximum trapping for finer textured bubbles. The trapped fraction, $X_t = 1 - X_f$, strongly influences the foam-flow resistance by reducing gas-phase relative permeability through eq. (10b).

To relate the flowing and trapped textures, we follow Friedmann *et al.* (1991) and assume local equilibrium. We argue that during coinjection of gas and liquid the trapped fraction is dynamic. Some of the trapped bubbles coarsen and remobilize to be replaced by subsequent trapping of flowing bubbles. Flowing and stationary texture are thus approximately the same. In the simulations to follow we set n_f equal to n_t.

Capillary Pressure

Capillary pressure is found via the Leverett J-function (Leverett, 1941). The following form of the J-function approximates the capillary pressure relation for our Boise sandstone

$$J(S_w) = \frac{P_c}{\sigma}\left(\frac{K}{\phi}\right)^{1/2} = \left(\frac{0.067}{S_w - 0.15}\right)^{0.2} \tag{13}$$

where ϕ is the rock porosity, K is the absolute permeability, and σ is the surface tension of the foamer solution.

Assumptions

To complete the model, phase-equilibria information is required. The aqueous surfactant phase is assumed to be incompressible and nonvolatile; the gas (i.e., N_2) in the foam phase is insoluble and obeys the ideal gas law. Further, it is assumed that when the core is presaturated with surfactant, the surfactant is present in equal concentration throughout the aqueous phase and that rock adsorption has been satisfied. In this instance, the surfactant mass balance is automatically obeyed. If the core is not presaturated with surfactant, we set rock adsorption to zero because the surfactant elution curves (Kovscek, 1994) for this clean sandstone display no significant adsorption loss. Also, it is assumed that once foam becomes trapped it cannot be displaced. This allows for simulation of so-called continuous-gas foams (Falls *et al.*, 1988).

Numerical Method and Parameter Fitting

The requisite conservation equations and constitutive relations are incorporated into a standard finite-difference simultaneous solution (SS) simulator with explicit upstream weighting of the phase mobilities for stability and solved (*c.f.*, (Aziz and Settari, 1979)). The four primitive unknowns are pressure, gas-phase saturation, surfactant concentration, and bubble density. Further numerical details are available elsewhere (Kovscek, 1994).

Table 1 lists the model parameters, nineteen in all excluding the capillary pressure relationship. Those applicable to standard, two-phase flow are shown to the left. They include the absolute rock permeability and porosity, phase viscosities, and Corey exponents and scaling constants for the continuum relative permeabilities. Information on the Boise core, including the relative permeabilities of nitrogen and water, is available from the experiments of Persoff *et al.* (1991). We fit eqs. (10) and (11) to those independently measured relative permeabilities.

Ten additional parameters are necessary to predict foam displacement, as listed to the right of Table 1. They include the generation and coalescence rate constants, the exponents a and b for the generation rate expression, the maximum limiting capillary pressure, $P^*_{c,max}$, the proportionality constant and velocity exponent for the foam effective viscosity, and the parameters for the trapped foam fraction. All parameters have clear physical meaning. Thus, the exponent for the effective viscosity, c in eq. (9) is set to 1/3 following extensions of the Bretherton analysis (Hirasaki and Lawson, 1985; Ginley, 1989). Also the theoretical calculations of Roof snap-off behavior in constricted, cornered pores (Kovscek, 1994) teach that $b = 1$ and that a is less than unity.

All but one of the remaining population-balance parameters are determined from steady-state behavior of foam flow, limiting the choice of parameter values. Thus, for our strong foamer solution at high salinity we choose $P^*_{c,max} = 30$ kPa (0.3 atm) and C^o_s of 0.083 wt% based upon the data of Aronson *et al.* (1994), and $X_{t,max} = 0.9$ based on the experimental tracer studies of trapped gas saturations (Friedmann *et al.*, 1991; Gillis and Radke, 1990).

Next, the exponent a is needed to specify the gas-velocity dependence of foam generation in eq. (4). In the limiting capillary pressure regime with strong foamers, the steady foam-flow pressure drop is sensibly independent of gas flow rate and varies linearly with liquid velocity (De Vries and Wit, 1990; Persoff *et al.*, 1991; Ettinger and Radke, 1992). When $r_g - r_c = 0$, eqs. (4) and (5) along with the foam-flow rheology

predicted by eqs. (8) and (9) reveal that a = 1/3, confirming the restriction of a < 1. The theoretical value of b = 1 demands a linear dependence of steady foam pressure drop on liquid velocity. The choices of a = c = 1/3 and b = 1 predict that foam texture must coarsen at higher gas velocity. This result, though not immediately obvious, is confirmed by experiment (Ettinger, 1989; Ettinger and Radke, 1992). We discover here that the origin of the unique flow behavior of foam in porous media is due to texture alteration with changing gas and liquid velocities, in addition to shear-thinning rheology. It is because of this changing texture that classical fractional flow theory ***does not*** apply to foam.

The important ratio, k_1/k^o_{-1}, sets the general magnitude of the bubble density. We choose steady-state textures on the order of 100 mm^{-3} or an equivalent undistorted bubble radius of about 130 μm, in agreement with the measurements of Ettinger and Radke (Ettinger, 1989; Ettinger and Radke, 1992). Equations (8) and (9) combined with steady-state texture now set the magnitude of the steady pressure drop and, consequently, α. It remains to specify the individual magnitudes of k_1 and k^o_{-1}. These are adjusted to confine the region of net texture refinement close to the inlet face of the porous medium (Ettinger, 1989; Ettinger and Radke, 1992). Thus, of the 10 population-balance parameters, 9 are preset by results of steady-state measurements. Finally, our simulations prove somewhat insensitive to the trapping parameter β, which is chosen such that $X_t = (1 - X_f)$ is 85% when n_f is 20 mm^{-3}.

In summary, the matching procedure requires only one steady-state pressure profile along with the accompanying steady-state trends of pressure drop versus gas velocity at fixed liquid rate and pressure drop versus liquid velocity at fixed gas rate. These are easily obtained within one experimental run. Once the foam displacement parameters are determined, there is no need to make adjustments to accommodate different types of transient injection or initial conditions. This feature makes our approach especially useful in scaling up from the laboratory to the field.

Steady Behavior

The results of the steady-state parameter matching procedure described above are shown as solid lines in Figs. 6 and 7. Figure 6 reports the steady-state system pressure drop versus liquid velocity at constant gas velocity while Fig. 7 displays the steady-state

pressure drop versus gas velocity (at exit pressure) relationship with liquid velocity held constant at two different levels.

In the steady state we find a good fit between experiment and theoretical prediction. In Fig. 6, the calculated pressure gradient increases linearly and overlies the experimental data (symbols) almost exactly. Figure 7 presents a fascinating result: pressure drop is independent of gas velocity at a given liquid rate. At the liquid velocity of 0.028 m/day in Fig. 7 (open circles) the foam simulator overpredicts the experimental pressure drop slightly, but matches almost exactly at a liquid velocity of 0.077 m/day. The overestimation of system pressure gradient is understood by comparing the constant liquid velocity used in Fig. 7 (0.028 m/day) with the results in Fig. 6. The experimental point at 0.028 m/day on Fig. 6 did not fall on the model predicted line. The data taken during that portion of the experiment appear to have slightly depressed pressure drops. In general, simulation mimics experiment well in the steady-state flow regime.

The steady-state pressure-drop trends are a result of the adjustment of foam texture as flow rates change. When gas velocity is varied under constant liquid flow rate conditions, foam texture coarsens, viscosity decreases, and constant pressure drop is maintained. When liquid velocity is increased while gas rates are held constant, foam texture increases linearly with v_w, and hence viscosity is adjusted so that apparent, incompressible Newtonian behavior is found.

Comparison of Theory and Transient Displacement Experiments

The following four test cases illustrate the efficacy of our population-balance method in reproducing a variety of transient foam-flow behavior. First, we consider two examples of simultaneous injection of gas and surfactant solution at different constant mass injection rates into a core completely saturated with surfactant solution. Next, we explore simultaneous injection of gas and surfactant solution, again at constant mass injection rates, into a core that is initially free of surfactant. Lastly, we inject gas at a fixed injection pressure into a surfactant-saturated core. In this case no liquid is injected.

In the transient flow regime, we wish to determine the length of time required for the system to come to steady state and to verify the existence and track the movement of foam displacement fronts within the porous medium.

Simultaneous Injection into a Surfactant-Saturated Core

In the first example, injection rates are quite low. Gas is injected at a rate of 0.43 m/day relative to the exit pressure of 4.8 MPa, and foamer solution is injected at 0.046 m/day into a surfactant-saturated core. This yields a quality or gas fractional flow of 90% at the core exit. Figures 8 and 9 display the model results in addition to the experimental saturation and pressure profiles. Figure 10 displays the foam texture profiles generated by the simulator. Unfortunately, no experimental method currently exists to measure directly foam texture *in situ*. The population-balance parameters employed here are identical to those above that reproduced steady-state foam behavior. Theoretical results are presented as solid lines. Dashed lines simply connect the individual data points. Elapsed time is given nondimensionally as pore volumes (PV) which is the ratio of the total volumetric flow rate (at exit pressure) multiplied by elapsed time and divided by the void volume of the core.

Steep saturation fronts are measured and predicted at all time levels in Fig. 8, whereby aqueous-phase saturation is roughly 30% (about 5 units above connate) upstream of the front, and 100% downstream. Model fronts are somewhat steeper and sharper than those measured experimentally, but the theoretical saturation profiles track experimental results very well. From the saturation profiles it is apparent that foam moves through the core in a piston-like fashion. After the front passes a particular location, saturation changes very little. Even though nitrogen and surfactant solution are injected separately, rapid foam generation and liquid desaturation still occurs very near the core inlet. Gas breakthrough at the core outlet occurs at roughly 1 PV, and little or no change experimentally or theoretically occurs in the saturation profile after breakthrough. Careful examination of Fig. 8 at x/L approximately equal to 1 reveals no evidence of a capillary end effect in the experimental saturation data.

The model further predicts that S_w is higher at the core inlet. Aqueous phase saturation is around 40% at x/L equal to zero, but drops rapidly to approximately 30% by x/L equal to 0.15. Since no foam is injected, foam bubble density is essentially zero at the inlet, effective flowing-foam viscosity is equal to the gas viscosity, and, consequently, S_w is higher than in the remainder of the core. Including the dispersive action of capillary pressure in the material balance fluxes obviates steep gradients in aqueous phase saturation. Without capillary pressure effects in the material balance fluxes, S_w is 76% at the inlet and drops to 30% by x/L equal to 0.20 (Kovscek, 1994). Minssieux (1974) detected such a region of high S_w near the inlet of a sandpack. A region of net foam

generation exists near the inlet by implication. Foam texture increases rapidly, but the region where rates of generation and coalescence are out of balance is finite. Unfortunately due to limited resolution, few experimental data are available in this region.

The region of net foam generation is also witnessed in the transient pressure profiles of Fig. 9. Both the experimental and model results (solid lines) show that pressure gradients near the inlet are shallow indicating that flow resistance is small. Steep gradients are found downstream of the inlet region. These steep gradients confirm the existence of a strong foam piston-like front moving through the core. Even though the gas fractional flow is quite high (90%) and the aqueous phase saturation is only roughly 30% in this downstream foam-filled region, the pressure gradients are linear indicating apparent incompressible foam behavior. In general, large pressure gradients are witnessed where aqueous-phase saturation is low and vice versa. Hence, we infer experimentally that foam texture must be coarse near the inlet and the fraction of foam flowing there is large.

These inferences are born out in Fig. 10 which reports model-predicted foam texture as a function of dimensionless distance and time. At all time levels, foam bubbles are coarsely textured near the inlet, but beyond the first fifth of the core, foam texture becomes nearly constant at each time level. Although *in-situ* textures cannot be measured, the magnitude of predicted foam textures, O(100 mm^{-3}), does agree with textures measured at the outlet face of a similar sandstone(Ettinger, 1989; Ettinger and Radke, 1992). Figure 10 also confirms that foam moves through the column in a piston-like fashion consistent with the experimental data in Figs. 8 and 9. Further consideration of these three figures shows that the saturation, pressure, and foam texture fronts track exactly both experimentally and theoretically. High pressure gradients and fine foam textures are seen where liquid saturation is low and vice versa.

We notice one more interesting feature of Fig. 10. At times equivalent to 0.65 and 0.80 PV, the bubble density downstream of the inlet region exceeds the foam texture at steady state. This effect arises because the compressibility of N_2 is included. A foam bubble created upstream finds itself out of equilibrium with the local pressure (*i.e.*, it is smaller or more dense than the local pressure demands) when it flows downstream. Hence, the steady-state texture is overshot somewhat as finely textured flowing foam fills the initially liquid-saturated regions near the foam front. Coalescence forces coarsen the bubbles over time to the equilibrium density. At steady state, the foam texture decreases

away from the inlet region. Essentially, the bubbles expand and hence their number density decreases as they flow downstream into lower pressure areas. No overshoot in bubble texture is found in the calculations when the gas phase is made incompressible (Kovscek, 1994).

The slight discrepancies between the experimental and model transient aqueous phase saturation and pressure profiles of Figs. 8 and 9 are easily understood. Resolution of the experimental aqueous phase saturation profiles is limited due to the finite time required to measure gamma-ray intensity at a station, and, also, the finite time required to measure saturation along the entire core. Thus, the experimental saturation fronts are smeared somewhat. Also transient pressures, in Fig. 9, are over predicted in some regions by roughly 100 kPa. Imposition of instantaneous equilibrium between flowing and trapped bubbles at early times may over predict the amount of bubble trapping, and consequently, flow resistance. Additionally, the proportionality constant for foam effective viscosity, α, increases with Plateau border curvature (Hirasaki and Lawson, 1985), and, hence, with decreasing water saturation. Accordingly, a constant value of α may over viscosify the foam at high S_w.

In the second example displayed in Figs. 11 to 13, foam displacement rates are roughly 3 times larger. Gas is injected at 1.2 m/day relative to the exit pressure of 5.0 MPa, and foamer solution is injected at 0.11 m/day again into a surfactant-saturated core where initially S_w is 100%. The gas fractional flow of 92% is slightly larger than in the first example. It is important to stress that model parameters are identical to those used to generate Figs. 6 to 10. Only the injection rates have changed.

Examination of Figs. 11 and 12 shows that, again, the experimental (symbols and dotted lines) and theoretical (solid lines) transient saturation and pressure profiles agree quite well. Sharp piston-like displacement is evident. Because higher rates are used, incurring a larger pressure drop across the core, and because the gas is compressible, the foam front progresses down the core more slowly than it did in the first example. In Fig. 8, gas breakthrough is somewhat after 0.80 PV, while in Fig. 11 it is closer to 1 PV. Again steady-state liquid saturation is higher at the core inlet and the pressure gradient is shallower than it is farther downstream in the core, due to the region of net foam generation near the beginning of the core. Figure 13 confirms that a piston-like front of foam develops that tracks exactly with the saturation and pressure profiles. The effects of compressibility on bubble texture are even more dramatic in Fig. 13 than they are in Fig. 10.

The apparent incompressible behavior of the foam at steady state evident in the pressure profiles of Figs. 9 and 12 is a unique result of the texture-dependent foam effective viscosity in eq. 9. At steady state the temporal derivative in eq. 1 is zero and the product of gas density and gas superficial velocity determines the gas-flow contribution to the pressure profile. Gas density and bubble texture both scale linearly with pressure. Thus, the ratio of gas density to foam effective viscosity is essentially independent of pressure.

Simultaneous Injection into a Brine-Filled Core

In Figs. 14 to 17, we report injection of gas and surfactant solution at fixed mass injection rates into a core completely saturated with brine containing no surfactant. The gas injection rate was 0.43 m/day while the foamer solution injection rate was 0.077 m/day to give a gas fractional flow of 85%. The system backpressure was 5.0 MPa. Because surfactant is not initially present throughout the core, a slower pressure response than the above two cases is anticipated.

In the transient theoretical saturation profiles shown in Fig. 14, we see that at short times (*i.e.*, 0.10 PV) two saturation fronts exist. The first front is located at roughly x/L equal to 0.35 and is the distance that unfoamed (*i.e.*, free) gas travels into the core. The experimental and theoretical locations of this first front agree well. Little liquid is displaced by this front because gas mobility is high in the absence of foam, and, consequently, gas breakthrough is quite rapid when the porous medium is not saturated with surfactant solution. The second front is at approximately x/L equal to 0.06 and is quite steep and sharp. This second saturation front corresponds to the distance of surfactant propagation. Foam forms quite rapidly when surfactant is present. This second saturation front is too close to the core inlet at a time of 0.10 PV to be detected experimentally.

After gas breakthrough, the foam piston-like front continues down the core expelling most of the liquid that the first displacement front left behind. Quite good agreement between simulation and experiment is witnessed even at the later times of 1.0 and 1.6 PV. Foam-front propagation is slow because foam transports only as quickly as surfactant. Foam coalescence is infinite whenever surfactant concentration is zero.

These points are well illustrated on Figs. 15 and 16. Figure 15 presents the transient foam texture profile whereas Fig. 16 contains the surfactant propagation profile. Comparison of these two figures shows that foam texture is quite fine when surfactant

concentration is high but declines dramatically where surfactant concentration is low. In the absence of any surfactant, foam texture is zero. In other words, a continuous channel of unfoamed gas exists.

Figure 17 presents the transient pressure profiles for this case. Because the theoretical saturation profiles track well with experiment, we expect the pressure profiles to track well also. Examination of Fig. 17 shows that this is indeed observed. Not only do theoretical and experimental foam-front locations in Fig. 17 match well, but also do the predicted and experimentally determined pressure gradients. Where saturation is low and surfactant concentration high, pressure gradients are quite steep and *vice versa.* As in the earlier cases, the pressure gradients near the core inlet are shallow reflecting the region of net foam generation near the core inlet shown in Fig. 15. The system pressure drop reaches steady state in about 3.5 PV.

Fixed Pressure Gas Injection

In the last mode of foam generation, shown in Figs. 18 to 20, gas alone is injected into a surfactant-saturated core such that foam is generated at a fixed pressure drop. Initially the experimental pressure drop established over the core was 380 kPa (55 psi). However, as gas discharged from the cylinder, the regulator allowed the pressure to fall to about 300 kPa (44 psi). The experimental decline in the injection pressure, seen in Fig. 18, was well documented, Thus, it was a simple matter to include a declining gas injection pressure into the numerical simulation of this experiment. Figure 18 displays the experimental and simulated pressure profiles. Examination of the system pressure drop at x/L equal to zero shows that the declining injection pressure was indeed accurately modeled. Because of the decline in injection pressure, choice of a gas flow rate for nondimensionalizing time is not clear. Roughly an hour after gas breakthrough, the effluent gas rate on the 0.1 MPa (1 atm) side of the backpressure regulator stabilized at 5.1 cm^3/s and remained constant. This rate is chosen to nondimensionalize time in both the experiment and simulation. Again the simulation parameters are identical to those used for the three earlier cases.

Figure 19 compares the experimental and simulated saturation profiles. Several features of this graph are worthy of note. First, the saturation profiles match moderately well. At times longer than 0.43 PV, the predicted front lags somewhat behind the experimental front, indicating that the simulated foam displacement is too efficient. Thus, the experimental saturation front is moving through the core more rapidly than is the

simulated one. Concomitantly, aqueous phase saturations upstream of the saturation front do not match as well as they did for the fixed-rate injection schemes. At 0.43 PV the theoretical saturation upstream of the front is slightly above 31%, whereas the actual average saturation is closer to 45%. After foam breakthrough, the experimental saturations continue to decline slowly as do the simulated ones. Given enough time, the experimental saturations, as well as the simulated ones, must decline to connate saturation, because no liquid is injected. In fact, the simulated profile at 3.8 PV indicates correctly that the core slowly dries out from the front towards the back. The actual experiment was not run long enough to reach connate liquid saturation and complete collapse of the foam.

Pressure profiles prior to foam breakthrough are shown in Fig. 18 at times of 0.18 and 0.43 PV. Again some discrepancies between the theoretical and actual pressure profiles are seen. In general though, the match between the two is acceptable. As suggested by the saturation profiles, the simulated pressure profile at 0.43 PV lags behind the actual profile. Careful study of Fig. 18 shows that the agreement at 3.8 PV is quite good.

When foam is generated with a fixed-inlet gas pressure, it is customary to also report the effluent gas rate at a variety of time levels to quantify gas production (Hanssen, 1993; Hanssen, 1993). For instance, at time levels of 1.1, 2.0, and 3.8 PV the experimental effluent superficial gas velocities are 0.24, 0.24, and 0.25 cm/s, respectively, while the model yields rates of 0.19, 0.21, and 0.21 cm/s. The difference between experiment and simulation here is consistent with the results discussed in Figs. 18 and 19. The simulator predicts a reduction in gas mobility that is slightly too large. This additional manner of comparison also shows that the theoretical model predicts foam behavior adequately.

Further examination of Fig. 18 reveals another interesting feature: the pressure gradients, both from experiment and simulation, are steepest immediately upstream of the foam front. Farther upstream the gradients lessen. The simulated bubble density profiles of Fig. 20 explain this behavior. Because only gas is injected and foam generation requires some liquid to be present in order for snap-off and lamellae creation to occur, foam texture coarsens rapidly far upstream of the foam front. Due to the reduced availability of liquid, foam generation cannot keep pace with coalescence, which is quite rapid because saturation is low, and correspondingly, the capillary pressure is large. At the displacement front, foam textures are fine (see the profiles at 0.18 and 0.43 PV)

because coalescence has not had time to catch up with generation yet. As the foam front moves through the core, foam texture at the front becomes coarser. This is a result of the gas advancing and causing a decline in the pressure drop through the gaseous phase, even though the injection pressure is remaining (fairly) constant. As a consequence, gas velocity and foam generation also decline. The bubble profile at 3.8 PV shows that given enough time, the flowing foam coalesces and the texture declines toward zero. Even if all flowing foam coalesces, a substantial portion of the porous medium contains trapped foam that impedes gas flow.

Conclusions

We have demonstrated that a foam displacement model based on the bubble population-balance approach well predicts experimental foam displacement under a variety of injection conditions in one-dimension. In general, we find good quantitative agreement between experiment and theory in both the transient and steady states. The numerical values of parameters required for the model are found by fitting steady-state trends and thus are not difficult to obtain. Hence, all simulated results shown here are produced from a single set of parameters. Because our population-balance formulation is mechanistic, it is general. Thus, extension to large field scales should be possible without parameter adjustment.

Direct incorporation of the role of foam texture into the simulator is the key to its success. Foam texture governs foam flow in porous media. A change in the flow velocity of either wetting liquid or gas must be accommodated by a change in texture and in turn a change in flow resistance. In transient and steady-state flow, fine foam textures lead to large pressure gradients and low liquid saturations, whereas coarse textures lead to lesser gradients and higher liquid saturations.

Specifically, we draw the following conclusions for foam displacement and flow in 1.3-μm^2 (1.3 D) Boise sandstone at 5 MPa backpressure and for total superficial velocities between 0.40 and 2.1 m/day.

When gas and liquid are injected simultaneously into a core initially saturated with aqueous surfactant solution, the resistance to gas flow builds rapidly in time. Steady state is generally achieved in about 2 PV, and the steady-state aqueous phase saturation is roughly 30%. The population-balance approach accurately predicts the location of saturation and pressure fronts.

When the porous medium is completely filled with brine but devoid of surfactant, the pressure response is slow. Two displacement fronts emerge. Unfoamed gas moves rapidly through those portions of the core where surfactant is absent. Where surfactant is present, foam forms, and the second displacement front builds. The second foam front tracks surfactant propagation through the core. Pressure gradients are large and saturations low where surfactant and foam are present and *vice versa*. Again, the population-balance approach mimics the experimental data.

When gas alone is injected into a core saturated with surfactant solution at a fixed pressure drop, a strong foam displacement front forms rapidly. The flow mobility of gas is reduced by the presence of foam during the displacement and for several PV after gas breakthrough. Although the simulator predicts a slightly larger reduction in gas mobility than is found experimentally, the agreement between the population-balance approach and experiment is quite good.

Finally, we find both experimentally and theoretically that a region of net foam generation exists very close to the inlet face of a linear core. Unfoamed surfactant solution and nitrogen are converted rapidly into a finely textured foam in this region.

Acknowledgment

P. Persoff provided invaluable assistance for the experimental program. This work was supported by the Assistant Secretary for Fossil Energy, Office of Oil, Gas, and Shale Technologies of the U.S. Department of Energy under Contract No. DE-AC03-76FS00098 to the Lawrence Berkeley Laboratory of the University of California.

Nomenclature

a,b,c	velocity exponents
C_S	surfactant concentration, wt%
f	wetting-phase relative permeability exponent
g	nonwetting-phase relative permeability exponent
I	intensity of gamma-ray beam (counts/sec)
J	Leverett J-function
k	rate constant, units depend on rate expression
k_r	relative permeability
K	permeability, m^2
L	length of core, m
n	number density of flowing foam (# of bubbles/volume of flowing foam)
p	pressure, Pa
PV	total pore volumes injected
P_C	capillary pressure, p_{nw}-p_w, Pa
Q	source/sink term in conservation equations (#/ time/volume)
r	foam generation or coalescence rate (#of bubbles/(time) (volume of gas))
S	phase saturation
u	Darcy phase velocity , m/s
v	interstitial phase velocity, m/s
x	distance, m
X	foam fraction

Greek Letters

α	proportionality constant for the effective viscosity of flowing foam
β	trapping parameter
ϕ	porosity
Π	disjoining pressure, Pa
σ	surface tension, N/m
μ	viscosity, Pa-s

Superscripts

o	reference value
*	limiting capillary pressure

Subscripts

1	generation rate constant
-1	coalescence rate constant
b	foam bubble
c	coalescence
f	flowing foam
fd	normalized flowing foam saturation
g	gas phase or generation
max	maximum or local maximum
nw	nonwetting phase
rup	rupture
s	surfactant
t	trapped foam
w	wetting phase
wc	connate saturation
wd	normalized wetting-phase saturation

References

Aronson, A.S., Bergeron, V., Fagan, M.E. and Radke, C.J., 1994, The Influence of Disjoining Pressure on Foam Stability and Flow in Porous Media. *Colloids and Surfaces A: Physicochemical Eng. Aspects* **83**, 109-120.

Aziz, K. and Settari, A., 1979, *Petroleum Reservoir Simulation*, Applied Science Publishers LTD, London.

Bear, J., 1988, *Dynamics of Fluids in Porous Media*, Dover, Mineola, N. Y.

Bergeron, V., 1993, *Forces and Structure in Surfactant-Laden Thin-Liquid Films*, Ph. D. Thesis, University of California, Berkeley.

Bergeron, V, Fagan, M.E. and Radke, C. J., 1993, Generalized Entering Coefficients - A Criterion for Foam Stability Against Oil in Porous Media. *Langmuir* **9**(7), 1704-1713.

Bernard, G.G. and Holm, L.W., 1964, Effect of Permeability of Porous Media to Gas. *Soc. Pet. Eng. J.* **4**(3), 267-274.

Bernard, G.G., Holm, L.W. and Jacobs, L.W., 1965, Effect of Foam on Trapped Gas Saturation and on Permeability of Porous Media to Gas. *Soc. Pet. Eng. J.* **5**(4), 295-300.

Bretherton, F.P., 1961, The Motion of Long Bubbles in Tubes. *J. Fluid Mech.* **10**, 166-188.

Chambers, K.T. and Radke, C.J., 1991, Capillary Phenomena in Foam Flow Through Porous Media. in *Interfacial Phenomena in Petroleum Recovery*, N. R. Morrow, Ed., Marcel Dekker Inc., New York, 191-255.

Chou, S.I., October, 1991, Condtions for Generating Foam in Porous Media. 66th Annual SPE Technical Conference, Dallas, TX, SPE 22628.

Corey, A. T., 1954, The Interrelation Between Gas and Oil Relative Permeabilities. *Producer's Monthly* **19**(1), 38-41.

De Vries, A.S. and Wit, K., 1990, Rheology of Gas/Water Foam in the Quality Range Relevant to Steam Foam. *Soc. Pet. Eng. Res. Eng.* **5**(2), 185-192.

Ettinger, R. A., 1989, *Foam Flow Resistance in Berea Sandstone*, M.S. Thesis, University of California, Berkeley.

Ettinger, R.A. and Radke, C.J., 1992, Influence of Foam Texture on Steady Foam Flow in Berea Sandstone. *Soc. Pet. Eng. Res.Eng.* **7**(1), 83-90.

Fagan, M. E., 1992, *The Stability of Foam and Pseudoemulsion Films and Foam Flow Through Glass Beadpacks*, M.S. Thesis, University of California, Berkeley.

Falls, A. H., Hirasaki, G. J., Patzek, T. W., Gauglitz, P. A., Miller, D. D. and Ratulowski, T., 1988, Development of A Mechanistic Foam Simulator: The Population Balance and Generation By Snap-Off. *Soc. Pet. Eng. Res. Eng.* **3(3)**, 884-892.

Falls, A.H., Musters, J.J. and Ratulowski, J., 1989, The Apparent Viscosity of Foams in Homogeneous Beadpacks. *Soc. Pet. Eng. Res. Eng.* **4(2)**, 155-164.

Friedmann, F., Chen, W.H. and Gauglitz, P.A., 1991, Experimental and Simulation Study of High-Temperature Foam Displacement in Porous Media. *Soc. Pet. Eng. Res. Eng.* **6(1)**, 37-45.

Friedmann, F. and Jensen, J.A., April, 1986, Some Parameters Influencing the Formation and Propagation of Foams in Porous Media. SPE California Regional Meeting, Oakland, CA, SPE 15087.

Gillis, J.V. and Radke, C.J., September, 1990, A Dual-Gas Tracer Technique for Determining Trapped Gas Saturation During Steady Foam Flow in Porous Media. 65th SPE Annual Technical Conference, New Orleans, LA, SPE 20519.

Ginley, G.M., 1989, Influence of Soluble Surfactants on the Flow of Long Bubbles Through a Cylindrical Capillary. in *Oil-Field Chemistry: Enhanced Recovery and Production Stimulation*, J. K. Borchardt and Yen, T. F., Eds., American Chemical Society Washington, D.C., 480-501.

Hanssen, J.E., 1993, Foam as a Gas-Blocking Agent in Petroleum Reservoirs. I:Empirical Observations and Parametric Study. *Journal of Petroleum Science & Engineering* **10(2)**, 117-134.

Hanssen, J.E., 1993, Foam as a Gas-Blocking Agent in Petroleum Reservoirs. II: Mechanisms of Gas Blockage. *Journal of Petroleum Science & Engineering* **10(2)**, 135-156.

Hanssen, J.E. and Dalland, M., April 1990, Foams for Effective Gas Blockage in the Presence of Crude Oil. 7th SPE Symposium on Enhanced Oil Recovery, Tulsa, OK, SPE/DOE 20193.

Hanssen, J.E. and Haugum, P., 1991, Gas Blockage by Non-Aqueous Foams. SPE International Symposium on Oil-Field Chemistry, Anaheim, CA, SPE 21002.

Hirasaki, G.J. and Lawson, J.B., 1985, Mechanisms of Foam Flow in Porous Media: Apparent Viscosity in Smooth Capillaries. *Soc. Pet. Eng. J.* **25(2)**, 176-190.

Holm, L.W., 1968, The Mechanism of Gas and Liquid Flow Through Porous Media in the Presence of Foam. *Soc. Pet. Eng. J.* **8(4)**, 359-369.

Huh, D.G. and Handy, L.L., 1989, Comparison of Steady- and Unsteady-State Flow of Gas and Foaming Solution in Porous Media. *Soc. Pet. Eng. Res. Eng.* **4(1)**, 77-84.

Jiménez, A. I. and Radke, C.J., 1989, Dynamic Stability of Foam Lamellae Flowing Through a Periodically Constricted Pore. in *Oil-Field Chemistry: Enhanced Recovery and Production Stimulation*, J. K. Borchardt and Yen, T. F., Eds.,American Chemical Society Washington, D.C., 460-479.

Khatib, Z. I., Hirasaki, G. J. and Falls, A.H., 1988, Effects of Capillary Pressure on Coalescence and Phase Mobilities in Foams Flowing Through Porous Media. *Soc. Pet. Eng. Res. Eng.* **3(3)**, 919-926.

Kovscek, A. R., 1994, *Foam Displacement in Porous Media: Experiment and Mechanistic Prediction by the Population Balance Method*, Ph. D Thesis, University of California, Berkeley.

Kovscek, A. R., Patzek, T. W. and Radke, C. J., October 1993, Simulation of Foam Transport in Porous Media. the 68th Annual Technical Conference of SPE, Houston, TX, SPE 26402.

Kovscek, A.R. and Radke, C.J., February 1993, A Comprehensive Description of Transient Foam Flow in Porous Media. DOE/NIPER Field Applications of Foams for Oil Production Symposium, Bakersfield, CA, No. FS-9.

Kovscek, A.R. and Radke, C.J., in press 1994, Fundamentals of Foam Transport in Porous Media. in *Foams in the Petroleum Industry*, L. L. Schramm, Ed.,American Chemical Society Washington, D.C.,

Leverett, M. C., 1941, Capillary Behavior in Porous Solids. *Trans., AIME* **142**, 152-169.

Mattax, C. C. and Dalton, R. L., Ed., 1990. Reservoir Simulation. SPE Monograph Henry L. Doherty Series. Richardson, TX, Soc. of Petr. Eng. of AIME.

Minssieux, L., 1974, Oil Displacement by Foams in Relation to Their Physical Properties in Porous Media. *J. Pet. Tech.* **26(1)**, 100-108.

Patzek, T. W., 1988, Description of Foam Flow in Porous Media by the Population Balance Approach. in *Surfactant-Based Mobility Control: Progress in Miscible-Flood Enhanced Oil Recovery*, D. H. Smith, Ed.,American Chemical Society Washington, D. C., 326-341.

Persoff, P., Radke, C.J., Pruess, K., Benson, S.M. and Witherspoon, P.A., 1991, A Laboratory Investigation of Foam Flow in Porous Media at Elevated Pressure. *Soc. Pet. Eng. Res. Eng.* **6(3)**, 365-371.

Ransohoff, T.C., Gauglitz, P.A. and Radke, C.J., 1987, Snap-Off of Gas Bubbles in Smoothly Constricted Noncircular Capillaries. *Am. Inst. Chem. Eng. J* **33(5)**, 753-765.

Ransohoff, T.C. and Radke, C.J., 1988, Mechanisms of Foam Generation in Glass-Bead Packs. *Soc. Pet. Eng. Res. Eng.* **3(2)**, 573-585.

Rossen, W.R. and Gauglitz, P.A., 1990, Percolation Theory and Mobilization of Foams in Porous Media. *Am. Inst. Chem. Eng. J.* **37(8)**, 1176-1188.

Rossen, W. R., to appear 1994, Foams in Advanced Oil Recovery. in Foams: Theory, Measurments and Applications, Prud'homme R.K. and Khan, S Eds. Marcel Dekker, New York.

Sanchez, J.M., Schechter, R.S. and Monsalve, A, October, 1986, The Effect of Trace Quantities of Surfactant on Nitrogen/Water Relative Permeabilities. 61st SPE Annual Technical Conference, New Orleans, LA, SPE 15446.

Stone, H. L., 1970, Probability Model for Estimating Three-Phase Relative Permeability. *J. Pet. Tech.* **22(2)**, 214-218.

Wong, H., Radke, C. J. and Morris, S., 1993, The Motion of Long Bubbles in Polygonal Capillaries: II. Drag, Fluid Pressure, and Fluid Flow. submitted to*J. Fluid Mech.*

Table 1: Parameter Values

Two-Phase Flow Parameters		Population Balance Parameters	
parameter	value	parameter	value
K	1.3 μm^2	k_1	1.4 E+5 $s^{1/3} cm^{-13/3}$
φ	0.25	k^o_{-1}	1.7 E-2 cm^{-1}
f	3.0	$P^*_{c,max}$	0.30 atm
k^o_{rw}	0.70	a	0.33
g	3.0	b	1.0
k^o_{rg}	1.0	α	4.0 E-6 mPa $s^{-1/3}$ $cm^{10/3}$
S_{wc}	0.25	c	0.33
μ_w	1.0 mPa·s	$X_{t,max}$	0.90
μ_g	0.018 mPa·s	β	1.0 E-3 cm^3
		C^o_s	0.083 wt%

Figure Captions

Figure 1: Pore-level schematic for a flowing foam. Flowing bubbles are unshaded and trapped gas is darkly shaded

Figure 2: Apparatus for foam displacement experiments.

Figure 3: Schematic of snap-off mechanism. Gas is unshaded. (a) Gas accumulation at pore throat, (b) Rearrangement of collar into a pore-spanning lens (c) Displacement of liquid lens after snap-off.

Figure 4: Foam coalescence in a periodically constricted pore. Coalescence occurs at t_3.

Figure 5: Schematic of generation and coalescence rates versus aqueous phase saturation. Arrows indicate how generation and coalescence rates shift with increasing interstitial velocity

Figure 6: Experimental (symbols) and model (solid line) steady-state pressure gradient versus liquid velocity at fixed gas injection rate. Typical error bars for experimental data are shown.

Figure 7: Experimental (symbols) and model (solid lines) steady-state pressure gradient versus gas velocity at fixed liquid injection rates. Typical experimental error bars are shown.

Figure 8: Experimental (symbols connected by dashed lines) and model (solid lines) transient aqueous phase saturation profiles. The porous medium is presaturated with surfactant solution.

Figure 9: Experimental (symbols connected by dashed lines) and model (solid lines) transient pressure profiles. The porous medium is presaturated with surfactant solution.

Figure 10: Model transient flowing-foam textures for a porous medium presaturated with surfactant solution.

Figure 11: Experimental (symbols connected by dashed lines) and model (solid lines) transient aqueous phase saturation profiles. The porous medium is presaturated with surfactant solution.

Figure 12: Experimental (symbols connected by dashed lines) and model (solid lines) transient pressure profiles. The porous medium is presaturated with surfactant solution.

Figure 13: Model transient flowing-foam textures for a porous medium presaturated with surfactant solution.

Figure 14: Experimental (symbols connected by dashed lines) and model (solid lines) transient aqueous phase saturation profiles. The porous medium is initially free of surfactant but saturated with brine.

Figure 15: Model transient flowing-foam textures for a porous medium initially free of surfactant.

Figure 16: Model transient surfactant concentration for a porous medium initially free of surfactant.

Figure 17: Experimental (symbols connected by dashed lines) and model (solid lines) transient pressure profiles. The porous medium is initially free of surfactant but saturated with brine.

Figure 18: Experimental (symbols connected by dashed lines) and model (solid lines) transient pressure profiles. Gas is injected at fixed pressure at core inlet. The porous medium is initially saturated with surfactant.

Figure 19: Experimental (symbols connected by dashed lines) and model (solid lines) transient aqueous-phase saturation profiles. Gas is injected at fixed pressure at core inlet.

Figure 20: Model transient flowing-foam textures. Gas is injected at fixed pressure at core inlet. The porous medium is initially saturated with surfactant solution.

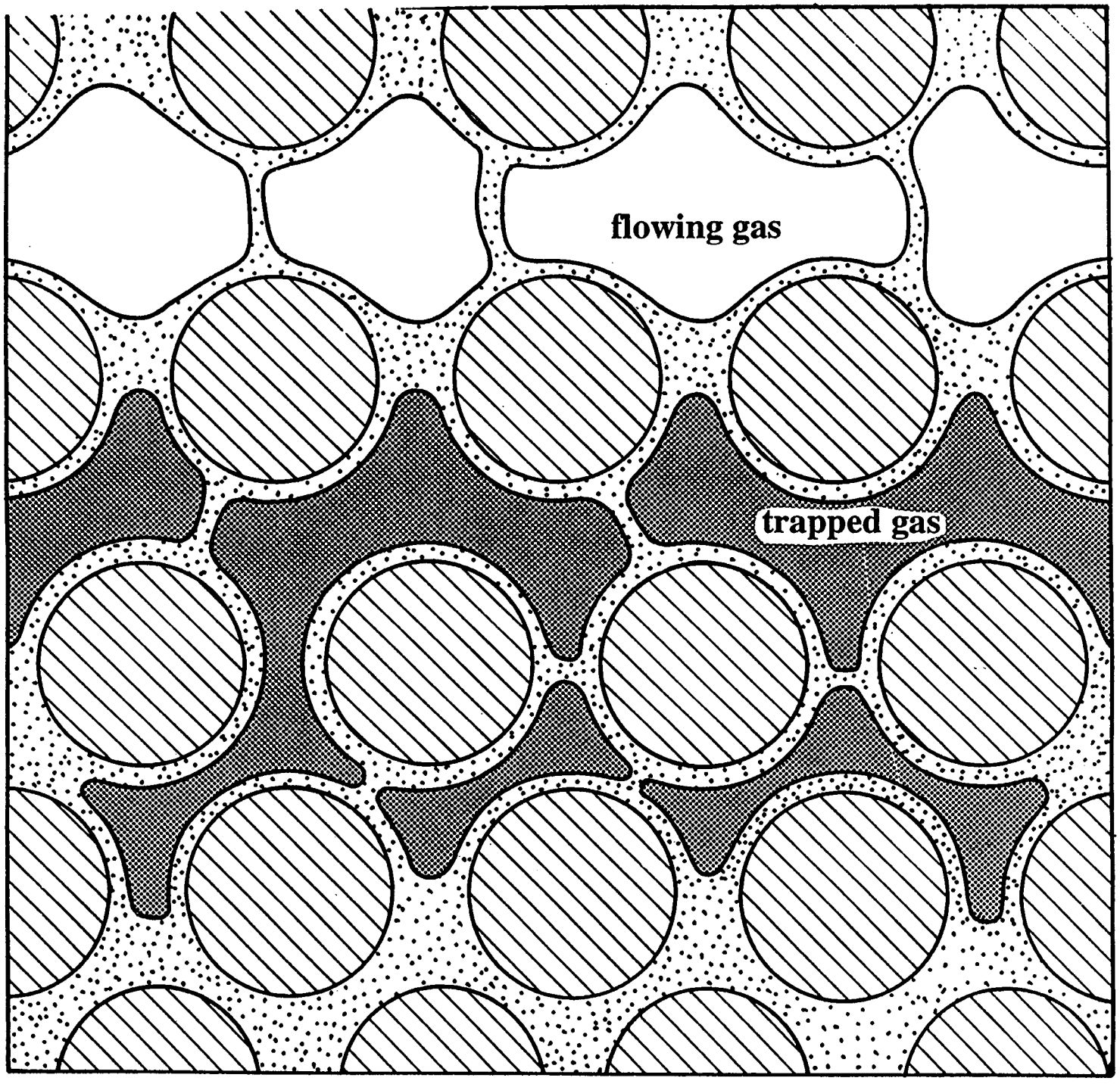

XBL 909-2973

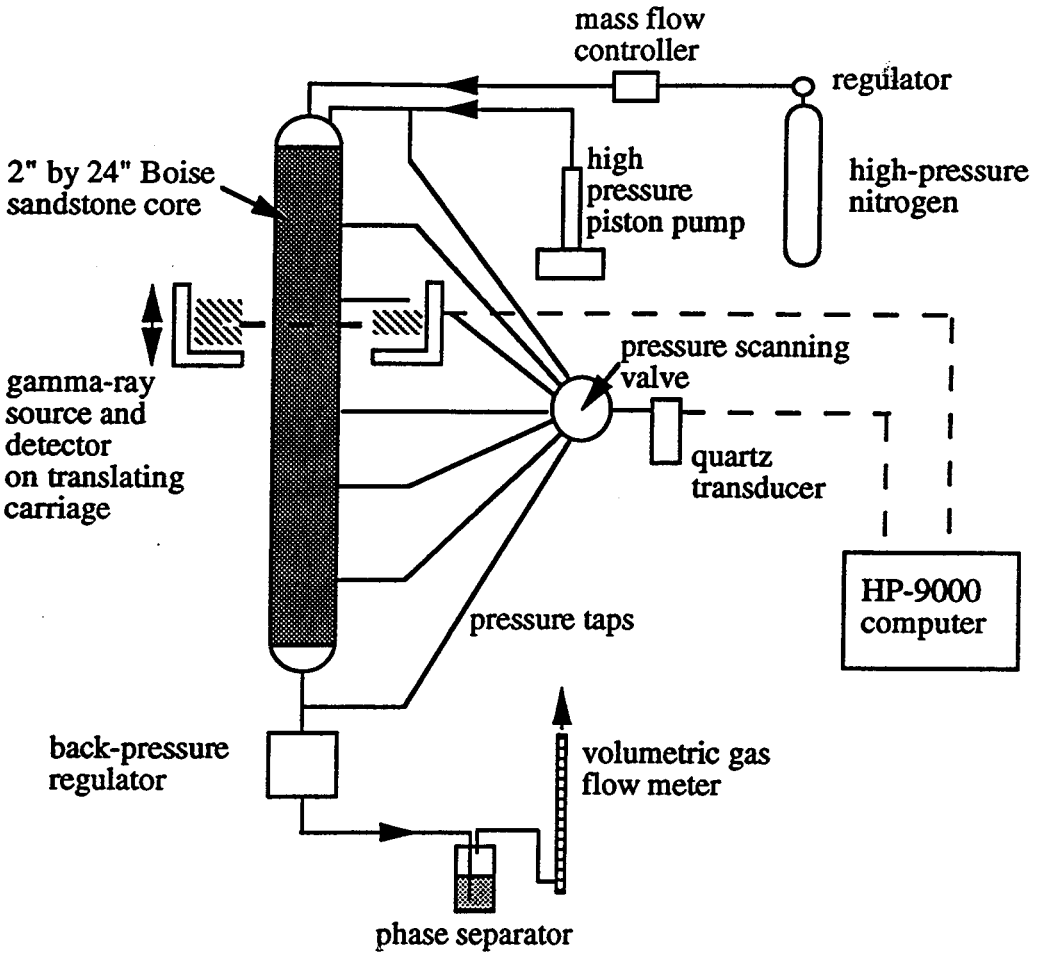

Figure 2. Kovscek, Patzek, and Radke

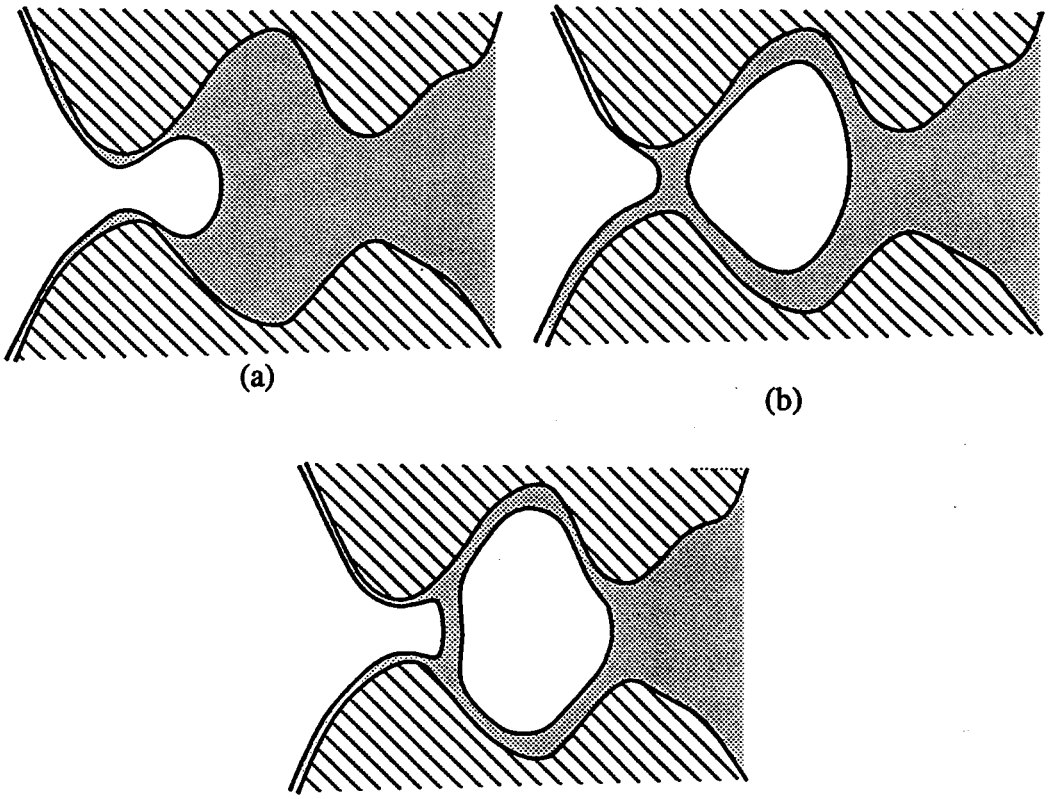

Figure 3 Kovscek, Patzek, and Radke

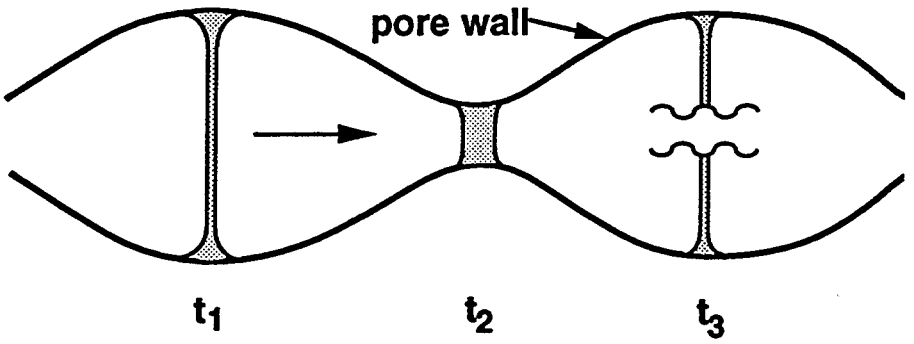

Figure 4 Kovscek, Patzek, and Radke

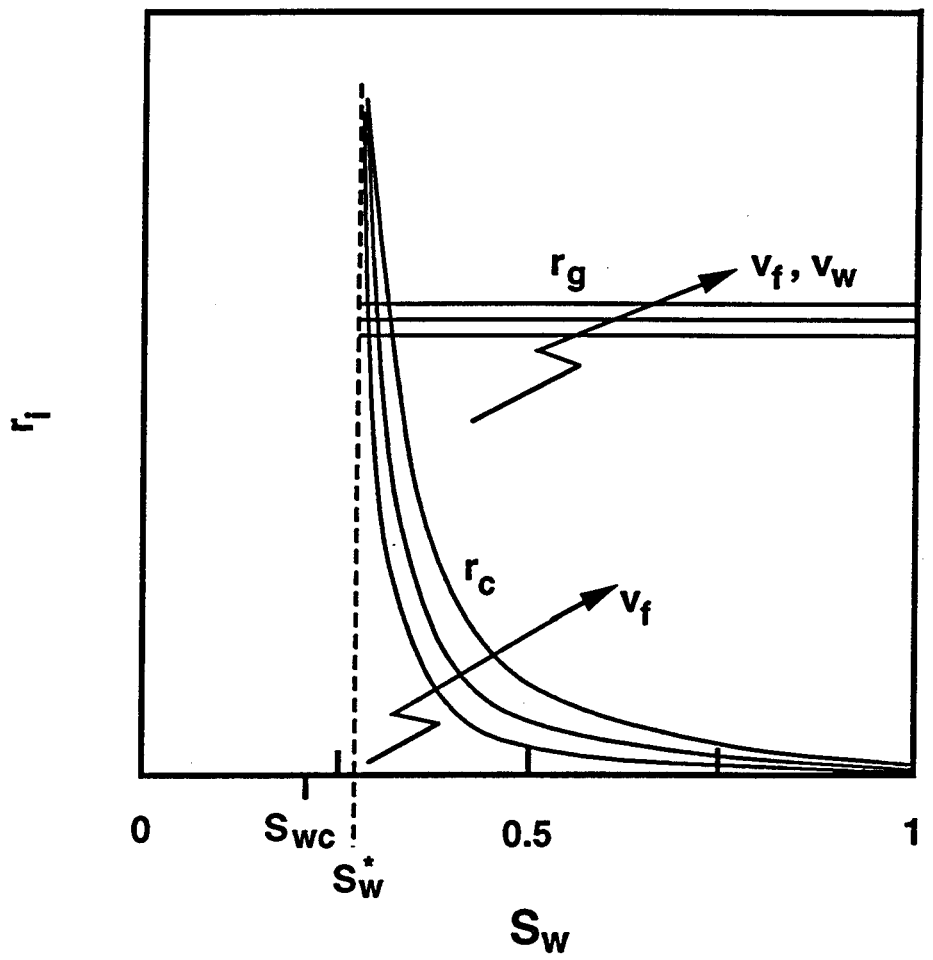

Figure 5 Kovscek, Patzek, and Radke

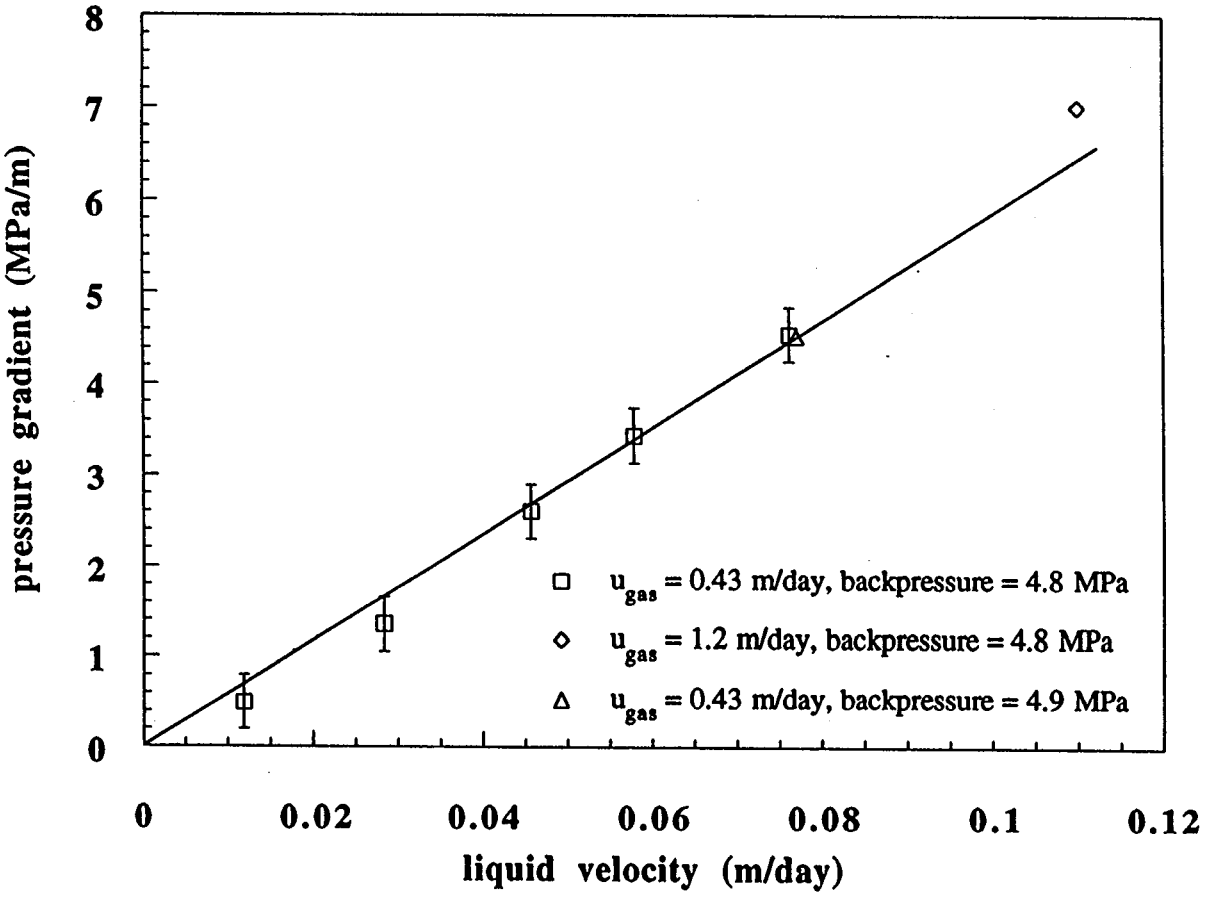

Figure 6 Kovscek, Patzek, and Radke

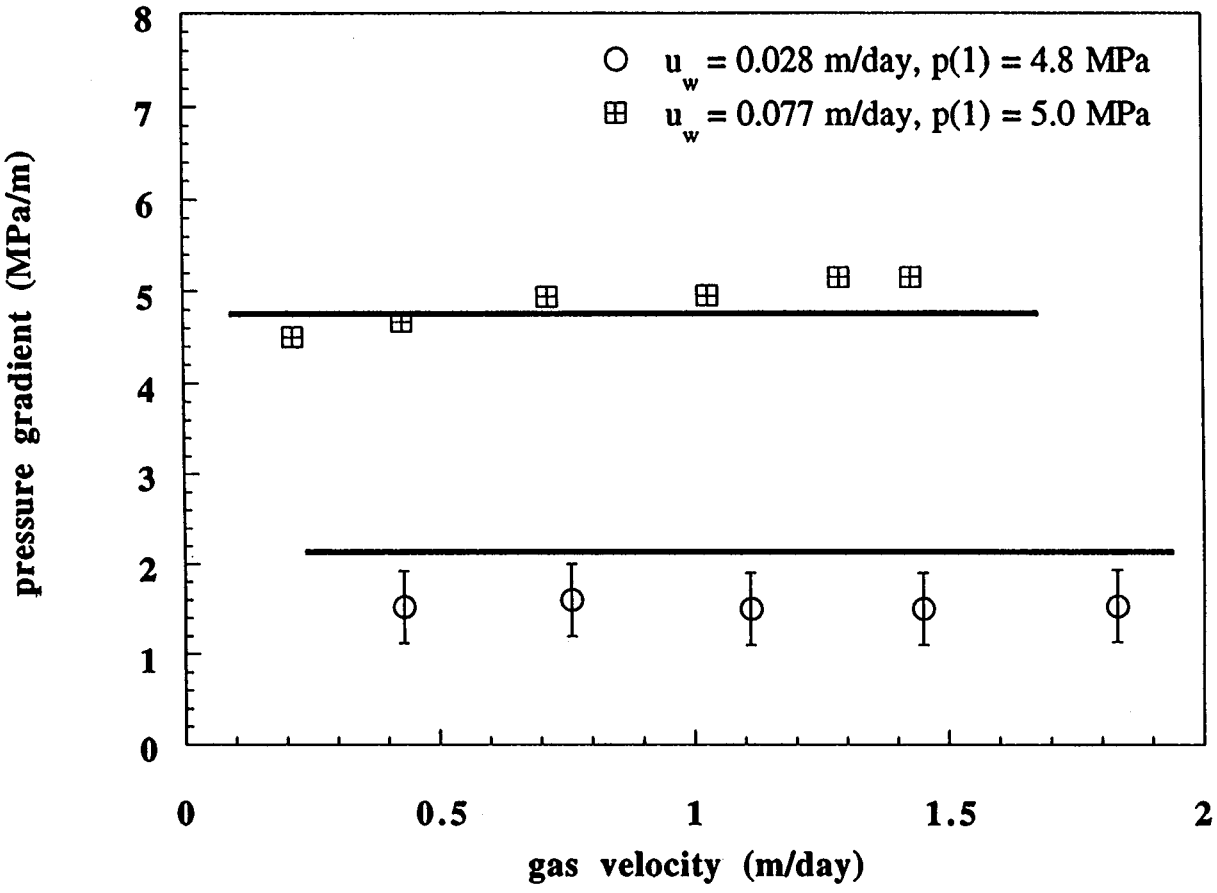

Figure 7 Kovscek, Patzek, and Radke

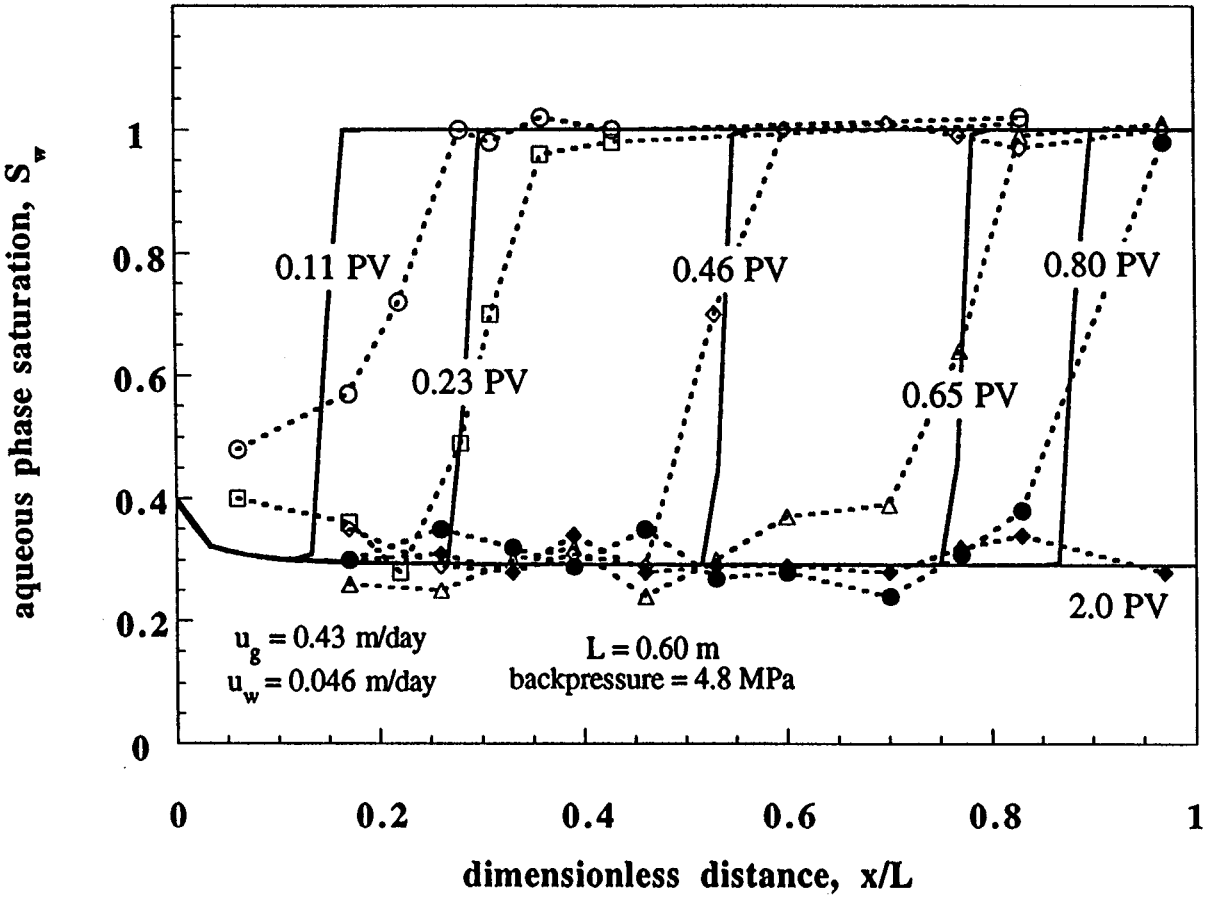

Figure 8 Kovscek, Patzek, and Radke

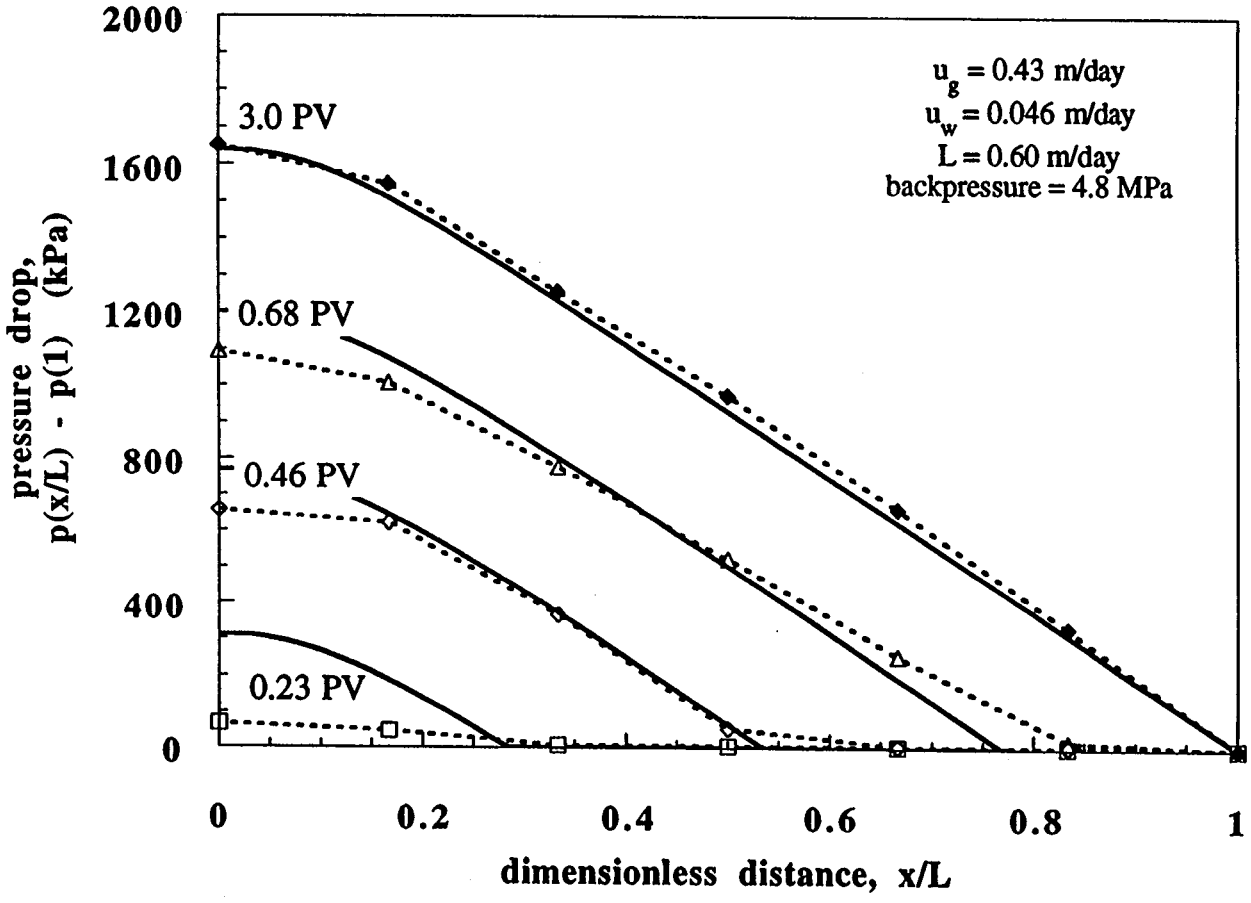

Figure 9 Kovscek, Patzek, and Radke

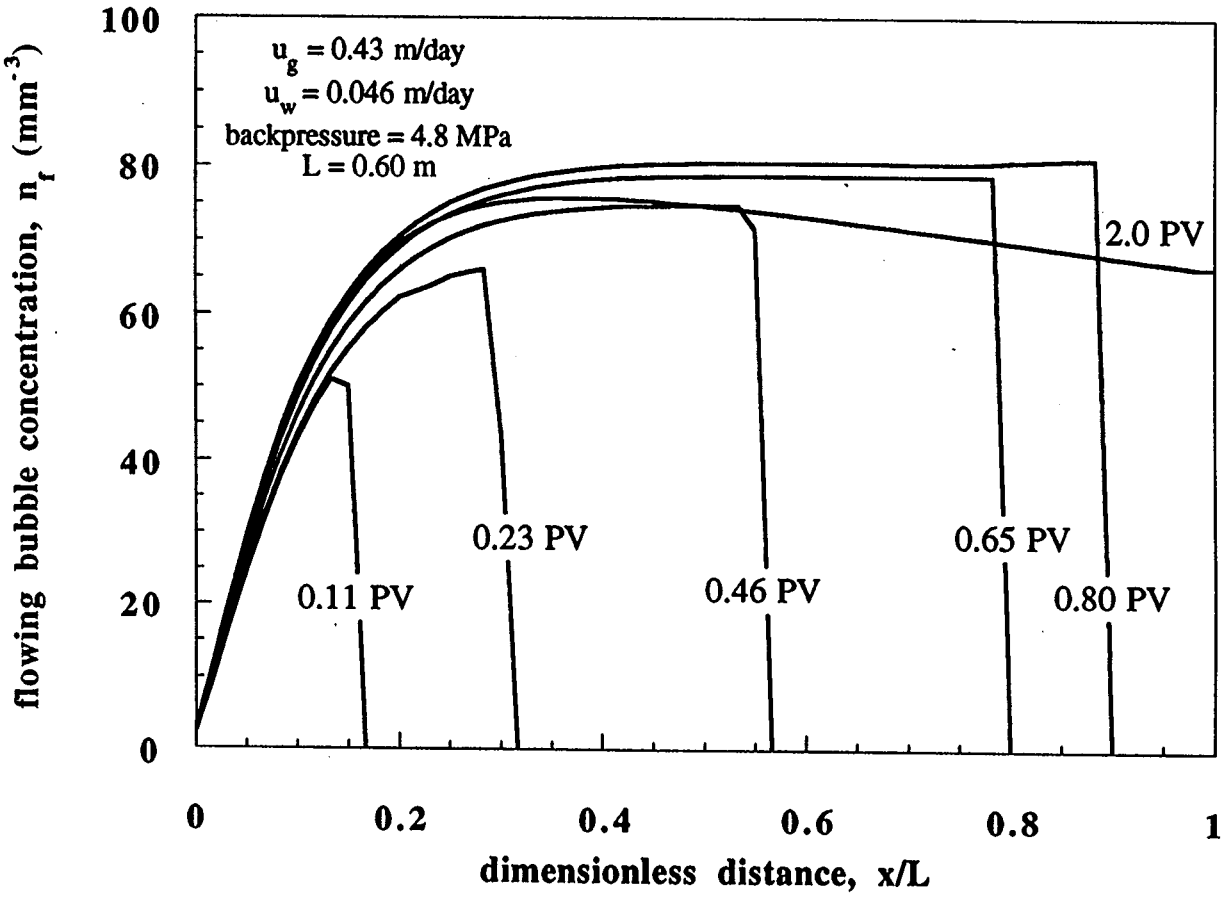

Figure 10 Kovscek, Patzek, and Radke

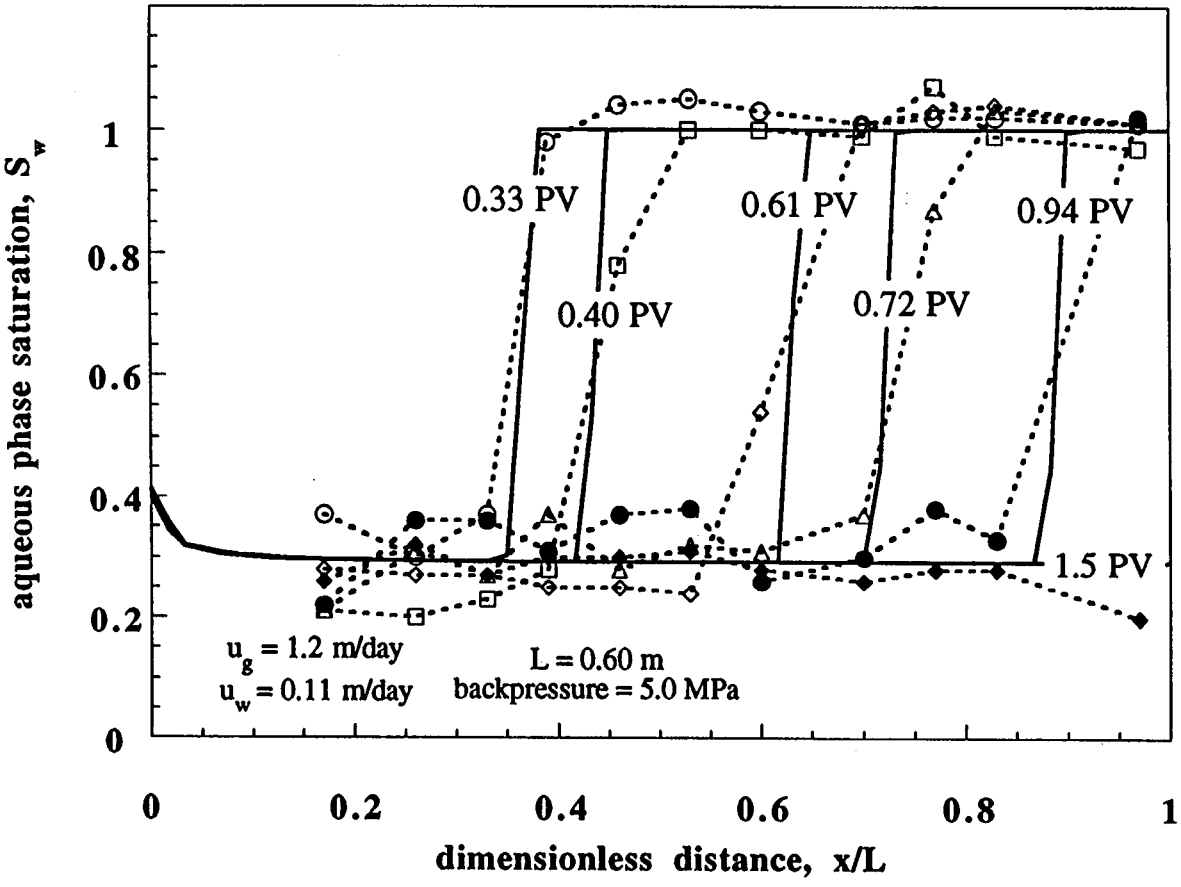

Figure 11 Kovscek, Patzek, and Radke

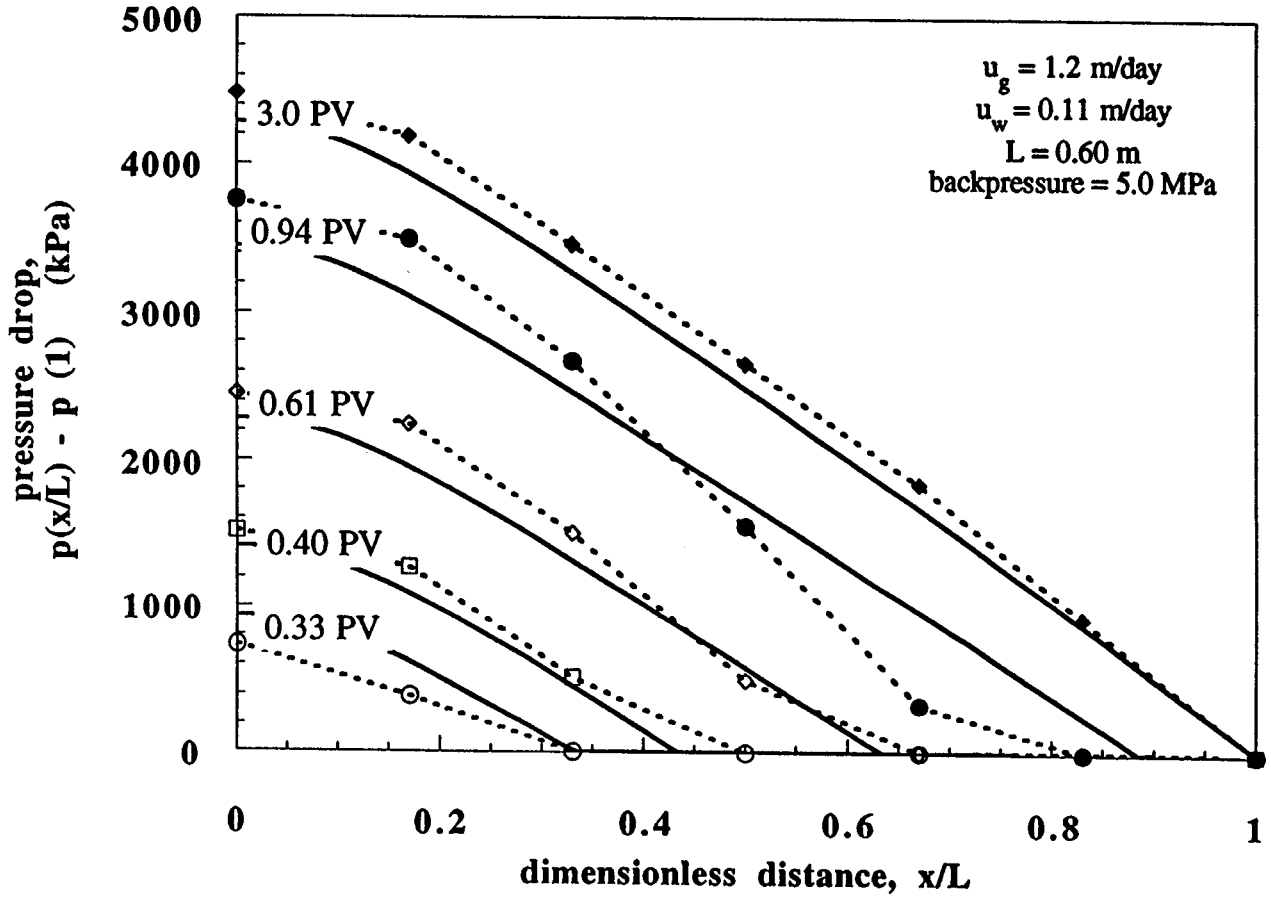

Figure 12 Kovscek, Patxzek, and Radke

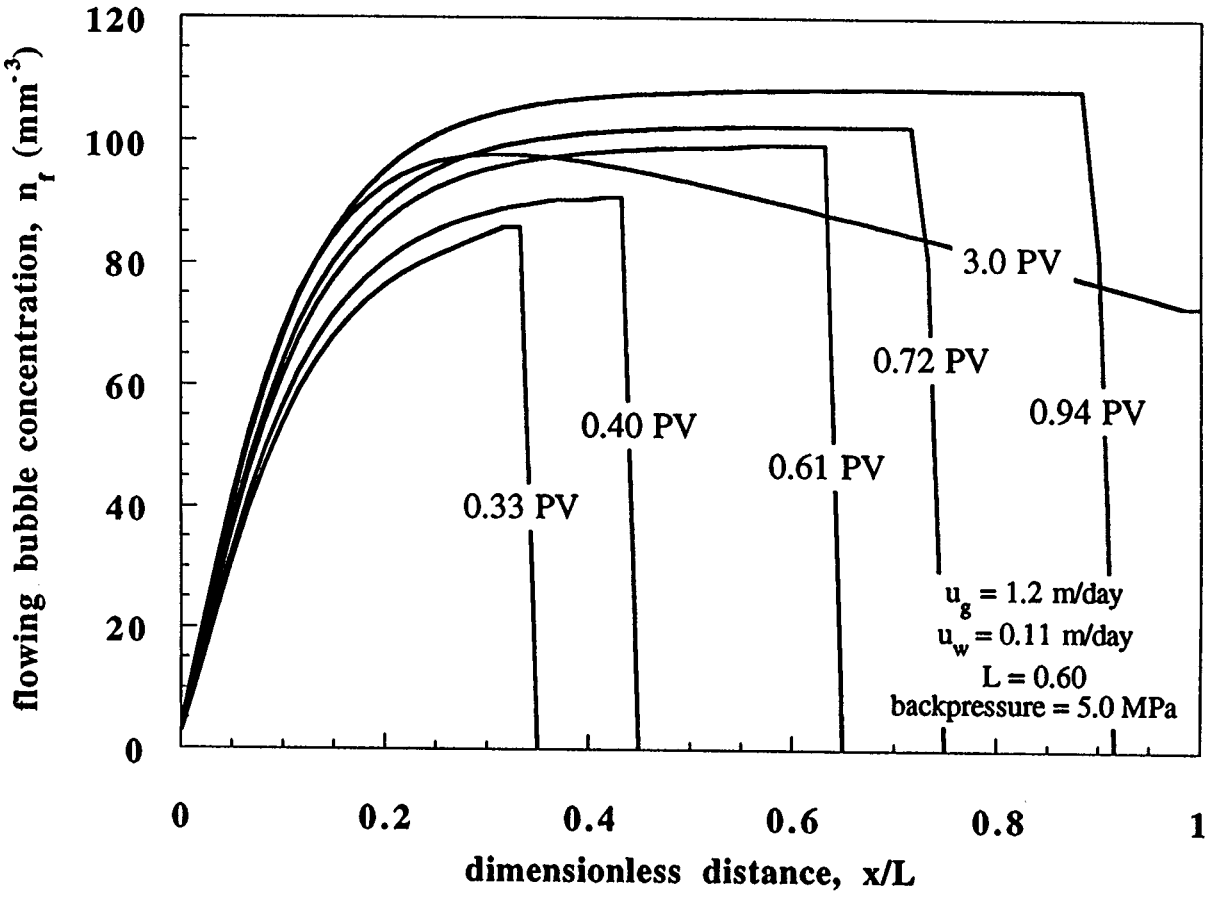

Figure 13 Kovscek, Patzek, and Radke

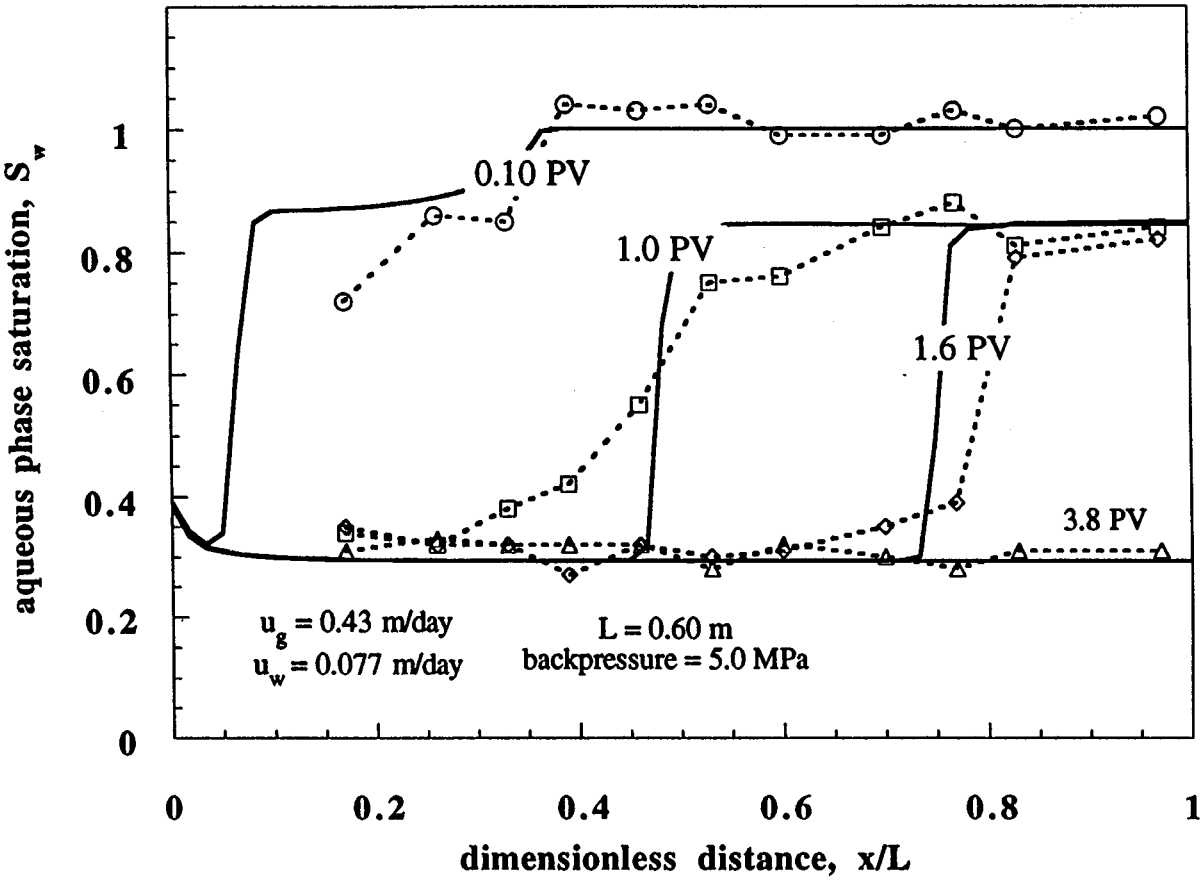

Figure 14 Kovscek, Patzek, and Radke

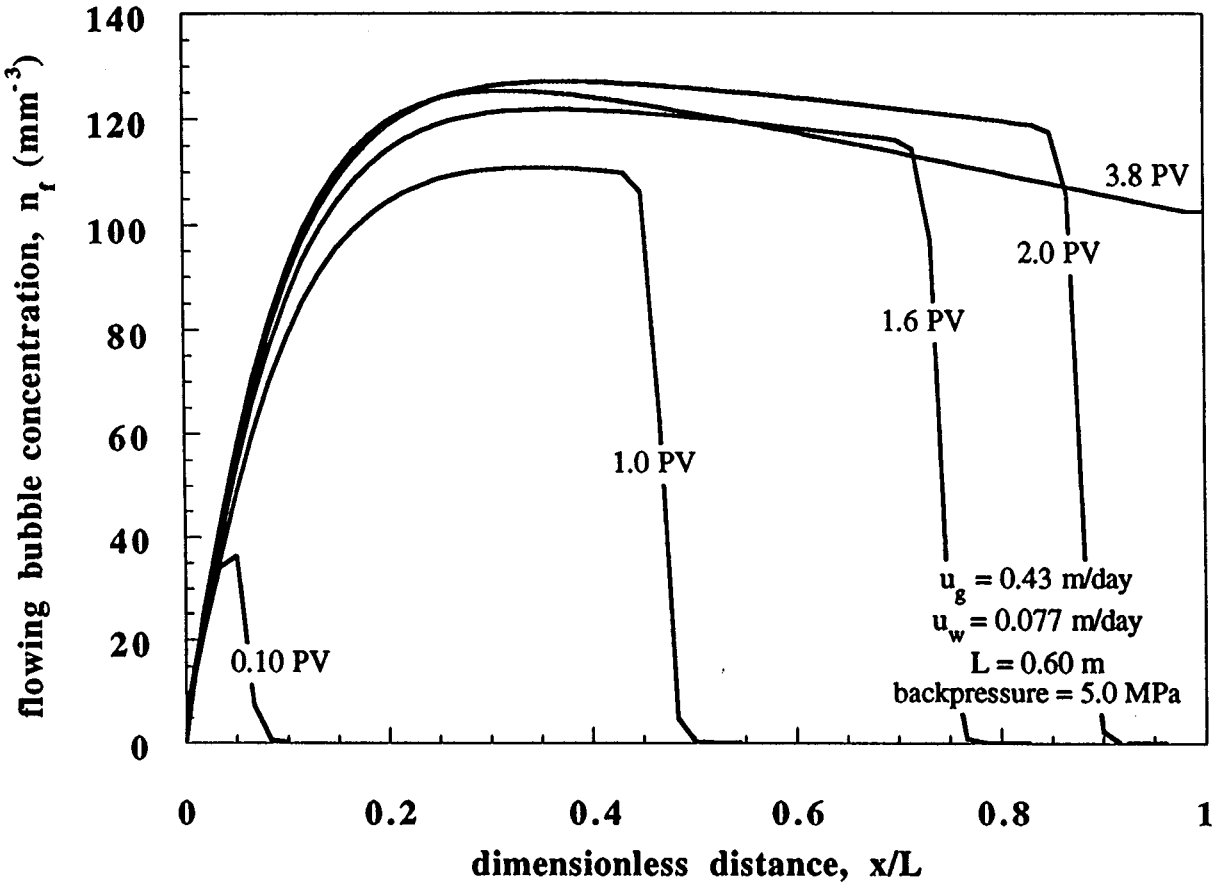

Figure 15 Kovscek, Patzek, and Radke

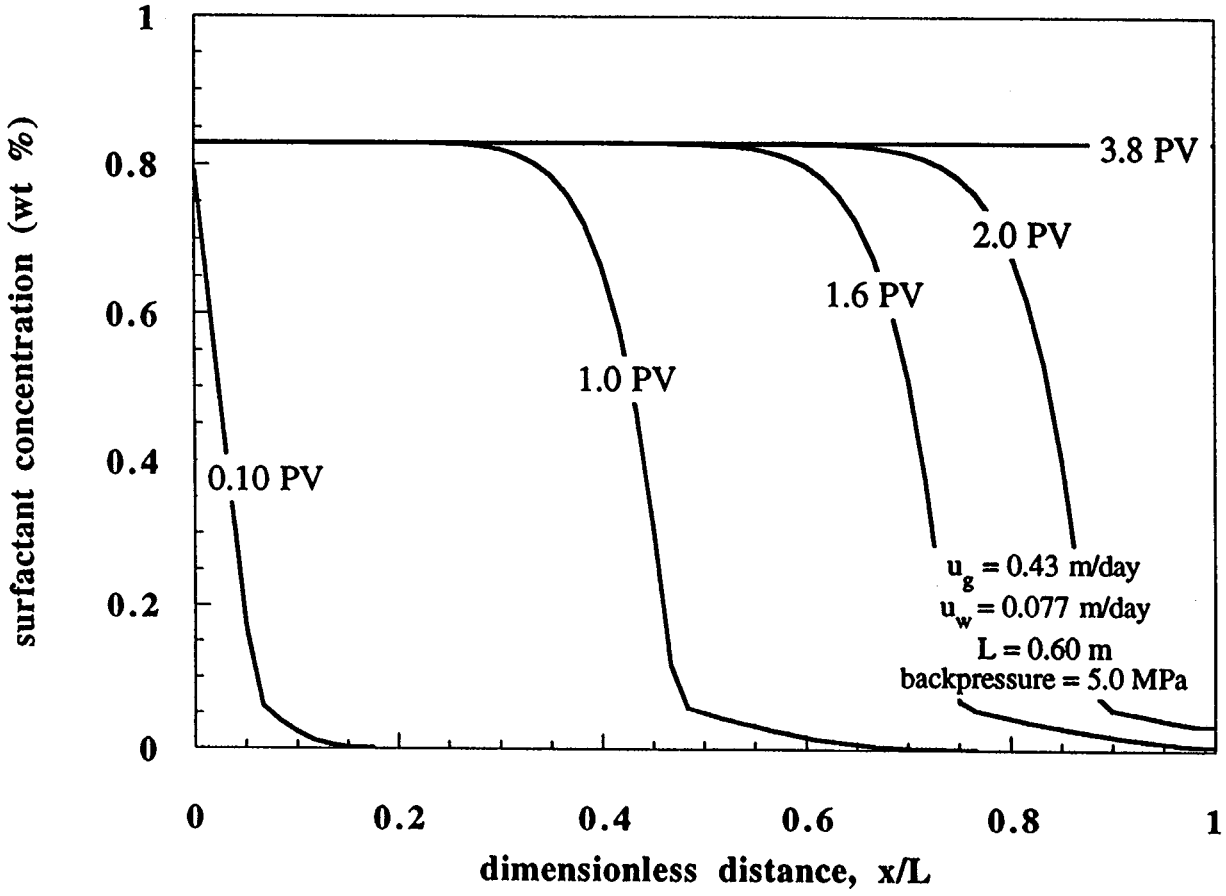

Figure 16 Kovscek, Patzek, and Radke

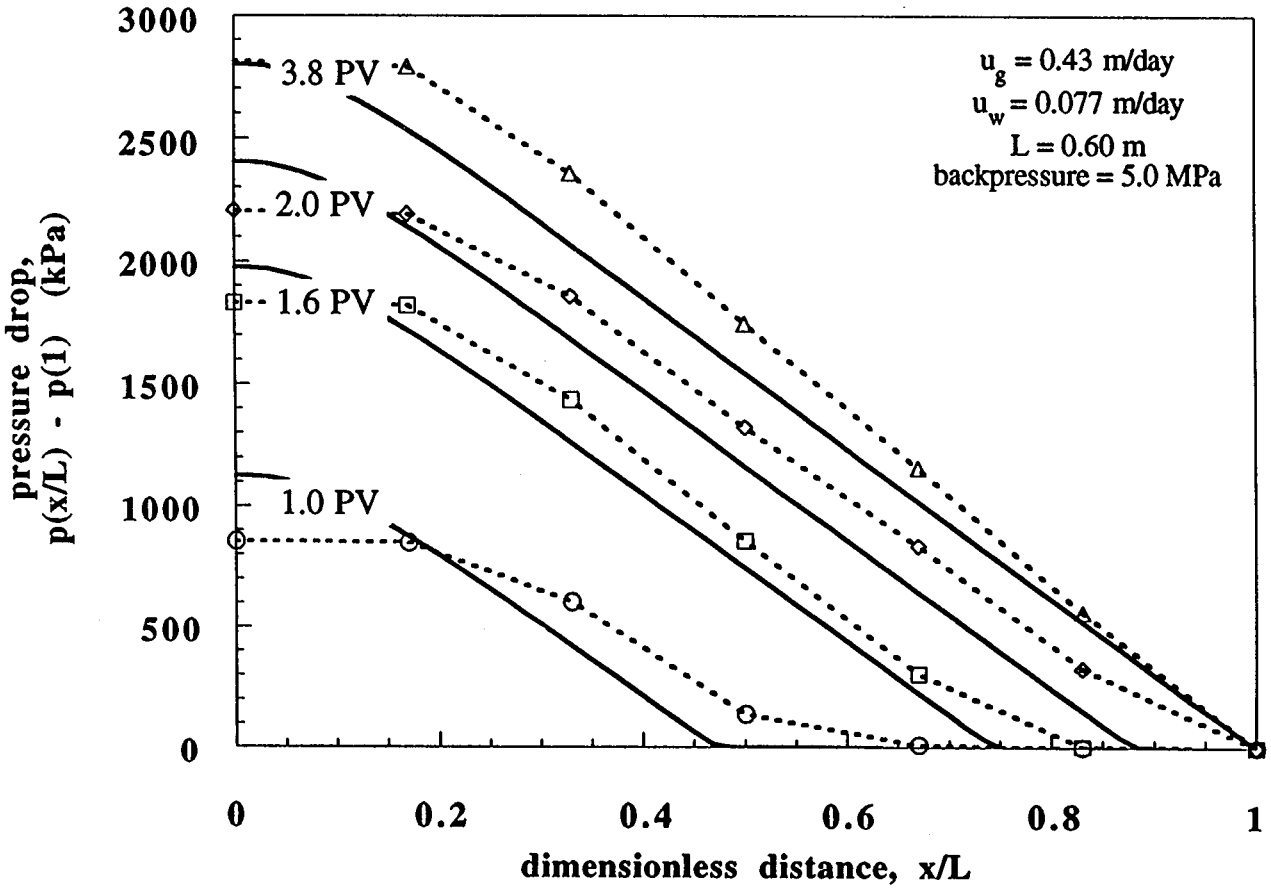

Figure 17 Kovscek, Patzek, and Radke

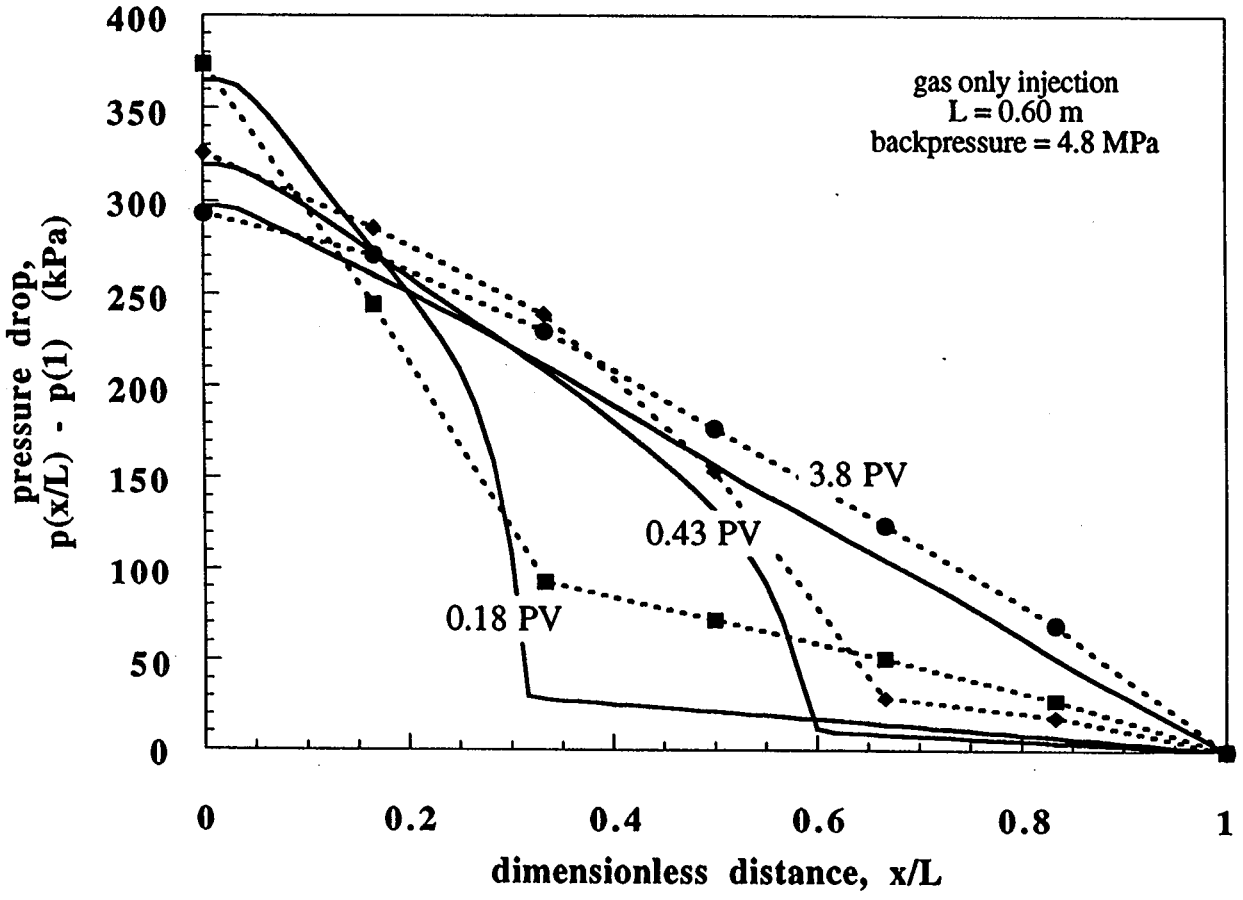

Figure 18 Kovscek, Patzek, and Radke

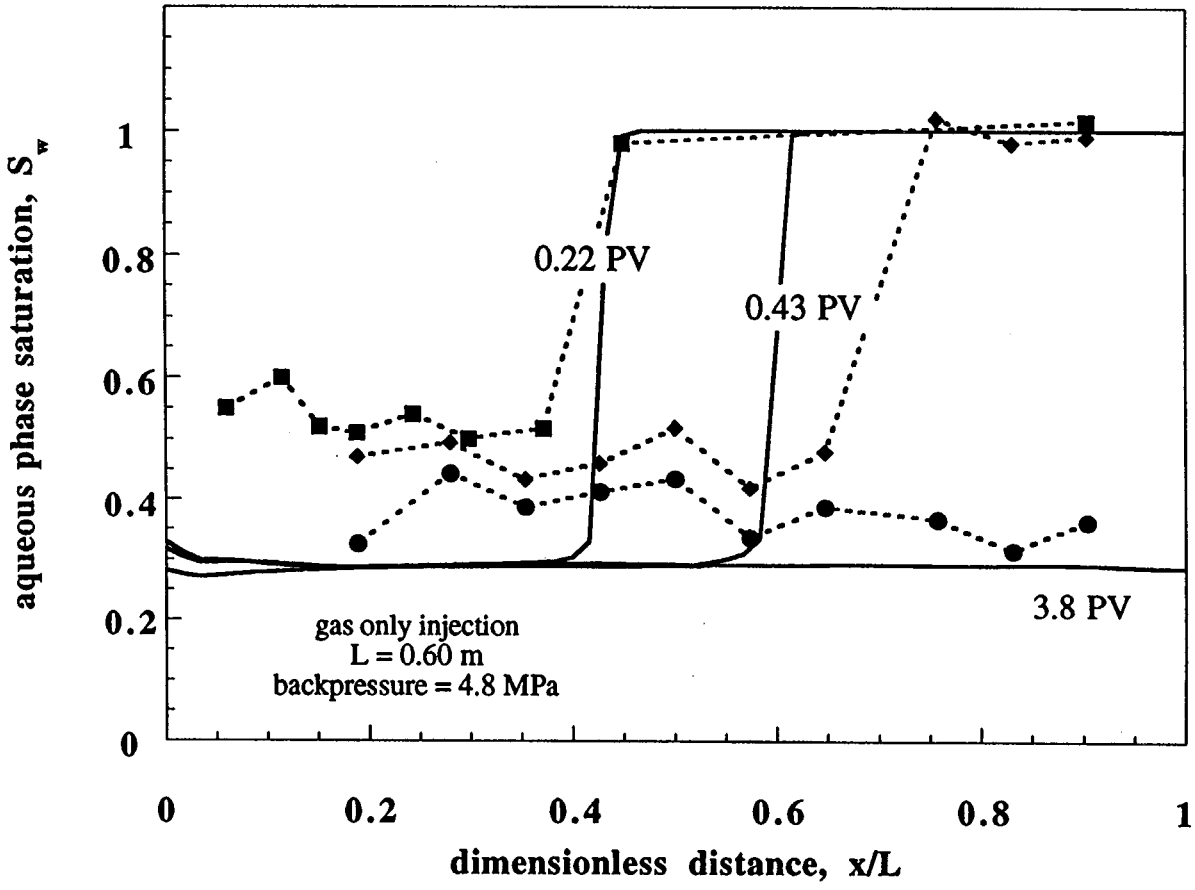

Figure 19 Kovscek, Patzek, and Radke

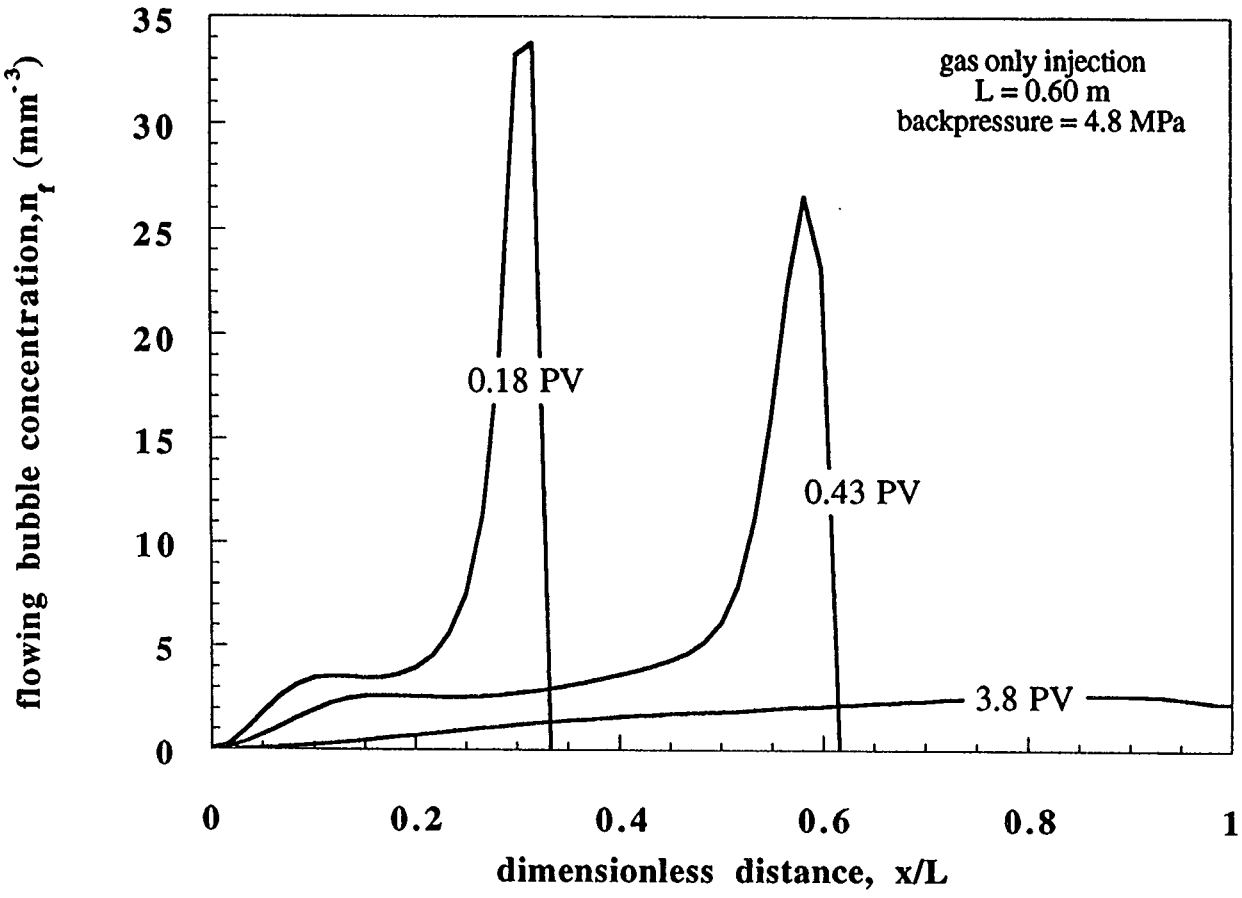

Figure 20 Kovscek, Patzek, and Radke

☆U.S. GOVERNMENT PRINTING OFFICE: 1995 - 660-029/20040